Moment method analysis of plane wave scattering from planar corrugated surfaces using parallel-plate cavity Green's functions and derivation of analytic reflection-phase formulas for both polarizations and oblique azimuth planes

M. Ng Mou Kehn[1]

Received 30 November 2011; revised 19 April 2012; accepted 22 April 2012; published 7 June 2012.

[1] A rigorous but yet highly accurate and efficient numerical treatment of plane wave scattering by T-shaped planar corrugations through full-wave modal analysis is first presented in this paper, which entails the moment method using parallel-plate waveguide cavity Green's functions and a numerical spectral-domain Green's function for planar stratified media. Investigations in terms of *both* reflection-phase and dispersion diagrams are conducted. After validating with the commercial software package: CST Microwave Studio, this moment-method is in turn used to verify a formula derived by the transverse resonance technique (TRT) for the surface-wave propagation constant of corrugations in terms of the dispersion diagram. Correspondences between the reflection-phase and dispersion diagrams are then established by relating the high and low impedance frequencies in the former with the pass and stop bands of the latter. With the abovementioned formula, the way is paved for a novel derivation of explicit formulas for the reflection-phase of an incident plane wave impingent on the corrugations as closed-form analytic functions of the various parameters, even for oblique azimuth planes of incidence and for both TE and TM polarizations. Doing so, the high or low surface-impedance (AMC or AEC) properties of such corrugations can virtually be acquired instantly, thus providing incomparable speedup of the process of thorough reflection-phase characterization of AMC or high-impedance surfaces and soft surfaces, thus affording rapid designs of antennas and microwave devices that make use of them.

Citation: Ng Mou Kehn, M. (2012), Moment method analysis of plane wave scattering from planar corrugated surfaces using parallel-plate cavity Green's functions and derivation of analytic reflection-phase formulas for both polarizations and oblique azimuth planes, *Radio Sci.*, *47*, RS3008, doi:10.1029/2011RS004938.

1. Introduction

[2] Corrugations have been an object of affectionate attention and keen interest among purists in electromagnetic theory for many decades. Dating as far back as to the 1940s, among the earliest works were accredited to *Goldstein* [1943, 1944], who investigated waveguides with corrugated metal walls. Another classical piece was by *Goubau* [1950], who in 1950, reviewed the work of *Sommerfeld* [1909] regarding axial surface waves on cylinders and extended the concepts by demonstrating that conductors with textured surfaces can support axial modes. And this was not long before the emergence of another seminal work by *Elliott* [1954], which studied the electromagnetic fields and propagation characteristics of a corrugated rectangular waveguide attached to a plane corrugated surface terminated by a ground plane. Shortly thereafter came along a pioneering paper by *Piefke* [1959], in which the transmission characteristics of a corrugated waveguide were analyzed under the assumption of electrically small corrugation period, allowing the structure to be replaced by a quasi-homogeneous but anisotropic medium whose permittivity and permeability are represented by tensors. And *Hougardy and Hansen* [1958] studied the surface wave propagation along an oblique angle with the orientation of the corrugations.

[3] The works of *Kalhor* [1976, 1977] in the seventies analyzed the scattering of electromagnetic waves from

[1]Institute of Communications Engineering, Department of Electrical and Computer Engineering, National Chiao Tung University, Hsinchu, Taiwan.

Corresponding author: M. Ng Mou Kehn, Institute of Communications Engineering, Department of Electrical and Computer Engineering, National Chiao Tung University, 1001 University Rd., Engineering Bldg. IV, Hsinchu 30010, Taiwan. (malcolmaxwell@gmail.com)

periodically corrugated conducting surfaces. Via matrix inversions, solutions were obtained by numerically solving systems of equations for the numerous unknown coefficients that expand the sought quantities (typically the fields). But yet, those methods still lacked full rigor and just gave approximate solutions, as further evidenced by *Kriegsmann and McCartin* [1996]. In *Kim et al.* [1999], a technique that hybridizes the method of moments with the uniform geometrical theory of diffraction (MOM/UTD) was presented for the analysis of corrugated surface-wave antennas with an infinite ground plane and fed by a parallel-plate waveguide. More recent works of *Uusitupa* [2006], *Hanninen and Nikoskinen* [2008], and *Alfonso et al.* [2009] described formulations based on the method of moments to analyze the scattering of impingent plane waves from corrugated surfaces.

[4] Theoreticians and computational enthusiasts were not the only ones captivated by this structure. Experimentalists and practical engineers in the microwave fraternity have, likewise for the past many years, been making use of corrugations to develop improved microwave devices such as waveguides and antennas. Most distinctively is the use of corrugations in synthesizing surfaces on which the behavior of electromagnetic waves can be controlled within specific frequency bands. Well known as soft and hard surfaces [*Kildal*, 1990] inaugurated at the dawn of the nineties, applications of such anisotropic surfaces are bountiful, e.g., reduction of the total scattered fields from metallic support struts of feeds in reflector antennas, curbing of cross-polarization of radiating slots in cylinders, suppression of undesirable mutual coupling and radiated sidelobes through reduced diffraction of surface waves from platform edges [*Li et al.*, 2005], as choke horn-feeds for paraboloids, just to name a few.

[5] These soft and hard surfaces bear a close relationship with the well-known electromagnetic bandgap (EBG) structure [*Yang and Rahmat-Samii*, 2008], whereby both demonstrate frequency bands within which the propagation of surface wave modes is permitted in some but prohibited in others. The primary difference between them lies in the anisotropy of the soft/hard surfaces, as in, surface-wave suppression in all directions is afforded by EBG structures but only over an angular span for corrugations, i.e., only along sector-limited directions. Important applications of EBG properties include the reduction of undesirable cross-talk between microwave components in the areas of EMC and IC packaging [*Mohajer-Iravani et al.*, 2006; *Kamgaing and Ramahi*, 2008; *Mohajer-Iravani and Ramahi*, 2007], suppression of losses due to mutual coupling in array antennas [*Yang and Rahmat-Samii*, 2003; *Farahani et al.*, 2010], as well as curbing edge diffraction from antenna structures thereby keeping the levels of sidelobe radiation under control. Perhaps the most famous example of an EBG structure is the so-called mushroom surface [*Sievenpiper et al.*, 1999]. Alternative configurations include patch arrays on grounded substrates [*Goussetis et al.*, 2006]. Not so widespread recognized, however, is that corrugations are also able to exhibit EBG behavior, particularly for the direction perpendicular to the gratings. This is tantamount to transverse corrugations, i.e., the soft surface.

[6] In the same way as the customary periodic array of patches printed on a grounded dielectric substrate [*Goussetis et al.*, 2006], corrugations are able to portray so-called artificial magnetic conducting (AMC) properties whereby the surfaces of the gratings exhibit high impedance values within certain frequency bands. Specifically, at frequencies where the phase of the reflection coefficient (or simply, reflection phase) of an incident plane wave on the corrugations falls between +90 deg and −90 deg, the surface is regarded as AMC or has high impedances. The frequency range over which this property prevails is then called the AMC bandwidth. Arguably, the most prominent application of this attribute is the realization of low-profile and conformal antennas. Others include the exploitation of the varying reflection-phases with angles of incidence, polarization, and frequency, to synthesize better ground planes for antennas [*Foroozesh et al.*, 2008a, 2008b].

[7] In virtue of the important roles which AMC and EBG characteristics play in many applications, two benchmark graphical representations of these properties have emerged in literature. They are the so-called reflection-phase and dispersion diagrams [*Goussetis et al.*, 2006]. However, despite the numerous studies on plane corrugations as outlined above, none of them has presented both the reflection-phase diagrams and dispersion diagrams *at the same time* and studied how these two could be related. It is thus among the main objectives of this paper to investigate corrugations via such graphical characterizations of their AMC and EBG behaviors and seek to discover linkages between them.

[8] Despite widespread mention and use in literature of the reflection-phase of periodic structures for studying HIS and AMC surfaces, none of them has provided explicit formulas for representing the reflection-phase for both principal polarizations and oblique azimuth planes of incidence as closed-form analytic functions of all parameters. However, in this paper, by using the transverse resonance technique (TRT) to derive an analytic functional form of the surface-wave number for TM polarization for surface propagation in the direction perpendicular to the corrugations, the *ultimate goal* here is to present a never-before seen derivation of a formulaic expression for the TM reflection-phase of a planar corrugated surface illuminated by a uniform plane wave as an analytical closed-form function of the numerous parameters of the corrugations (such as the depth, material of the groove filling, period, etc), the angular direction of the incident wave (represented by θ_{inc} and ϕ_{inc}), as well as the frequency. This remarkably innovative method for obtaining an explicit formula for the TM reflection phase allows for instantaneous (as opposed to heavy full-wave computational simulations) but yet highly accurate determination of the reflection-phase properties of planar corrugated surfaces, by direct evaluations of the abovementioned derived analytic function without even the need to carry out a single rigorous computational solution of the structure. The importance and usefulness of such a formula do not need any further emphasis or justification. This above derivation shall then be extended to obtain the reflection-phase formula for the TE case as well.

2. Theoretical Formulation: Full-Wave Moment Method Treatment

[9] Before commencing the analysis, it is worth justifying its value by saying that, although *Uusitupa* [2006], *Hanninen and Nikoskinen* [2008], and *Alfonso et al.* [2009] also dealt with plane wave scattering of corrugated surfaces using the moment method, they all suffer from shortcomings which this presently proposed approach does not. Compromise of rigor and robustness is sustained by the approach of *Uusitupa* [2006] which utilized restrictive slab models, whereas the method proposed

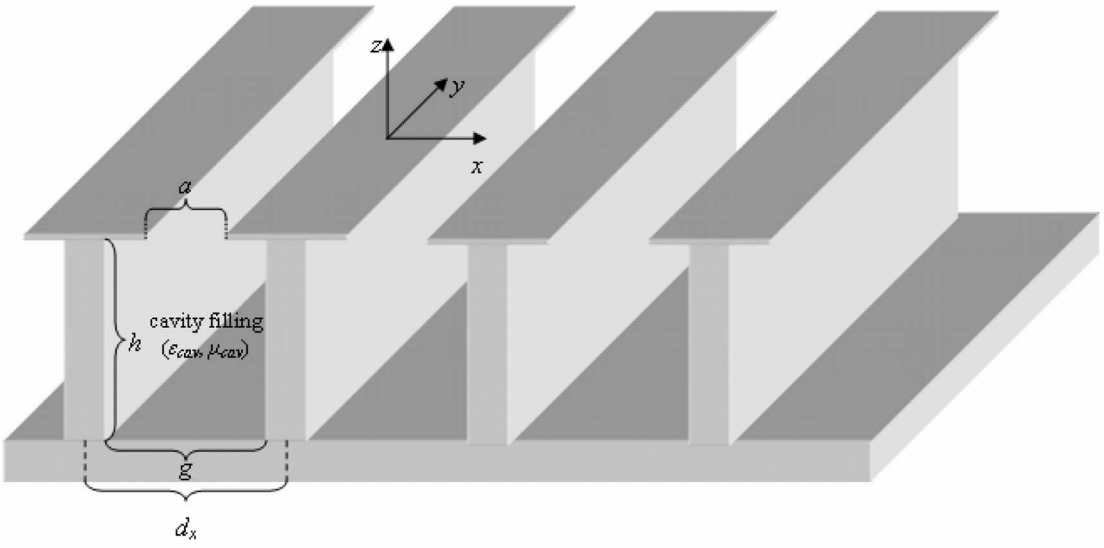

Figure 1. Corrugations with metal fin-plate over each ridge to form T-shaped corrugations.

in *Hanninen and Nikoskinen* [2008] is after all still only an approximated one due to the impedance boundary condition used. The accuracy of the treatment in *Alfonso et al.* [2009] of finite corrugated surfaces is limited by the coarse modeling of the equivalent magnetic current over the aperture of the corrugations with sub-domain rooftop basis functions (as opposed to entire-domain modal ones). Moreover, *Alfonso et al.* [2009] have restricted the analysis to magnetic current flow only along the groove aperture and neglected the component perpendicular to the corrugations, rendering the method unsuitable for managing gratings with wider grooves. The need to treat each of the numerous apertures of the finite corrugations individually also makes that approach cumbersome. On the contrary, the present full-wave method is elegant, fully rigorous, and based on classical theories of surface equivalence and Green's functions derived from the reciprocity theorem, being able to treat corrugations with grooves and ridges of any thickness. The only approximation sustained is the truncation of the number of entire-domain modal basis functions, an aspect no numerical technique can avoid.

[10] The planar corrugated surface to be analyzed is shown in Figure 1. An extended and more general form of corrugations is herein considered, whereby a horizontal metallic strip plate is now placed over each vertical ridge to form the so-called T-shaped corrugations. When the strip-width equals the ridge-width, thus shedding the iris-type apertures, this T-type version then simplifies (specializes) to conventional corrugations. The analysis is divided into the following steps: (A) initialization with orthonormalized parallel-plate waveguide modes, (B) expansion of infinitely long PEC-equivalent magnetic aperture strip currents into parallel-plate waveguide (PPW) modal basis functions, (C) obtaining the *H*-fields radiated into the grooves via PPW cavity Green's function, (D) Fourier transform of the PEC-equivalent magnetic strip-current over the iris-type aperture, (E) acquiring the spectral-domain magnetic fields radiated by spectral-domain basis magnetic currents located on the surface of the infinite PEC ground plane, (F) obtaining the spatial-domain fields radiated by the entire array of magnetic strip currents into the region above the corrugations, (G) enforcement of the boundary conditions requiring the continuity of tangential *H*-fields across the PPW cavity aperture, (H) Galerkin weighting and construction of intermediate matrices, and (I) matrix operations and construction of the ultimate moment-method matrix equation to be solved via matrix inversion for the unknown amplitude coefficients expanding the magnetic strip currents.

2.1. Orthonormalized Parallel-Plate Waveguide Modes

[11] Consider first, the following parallel-plate waveguide (PPW) in Figure 2. The orthonormalized PPW eigenmodal field functions for TM^z and TE^z modes are then written as follow.

$$e^{\{^{cav}_{ap}\}}_{x_s,\mathrm{TM}^z} = -\sqrt{\frac{\kappa_s \gamma^{\{^{cav}_{ap}\}}_{z_s}}{j\omega\varepsilon_{\{^{cav}_{ap}\}}\{^{g}_{a}\}}}\cos\left(\frac{s\pi x}{\{^{g}_{a}\}}+\frac{s\pi}{2}\right) \tag{1a}$$

$$e^{\{^{cav}_{ap}\}}_{z_s,\mathrm{TM}^z} = \frac{s\pi}{\{^{g}_{a}\}}\sqrt{\frac{\kappa_s}{j\omega\varepsilon_{\{^{cav}_{ap}\}}\{^{g}_{a}\}\gamma^{\{^{cav}_{ap}\}}_{z_s}}}\sin\left(\frac{s\pi x}{\{^{g}_{a}\}}+\frac{s\pi}{2}\right) \tag{1b}$$

$$h^{\{^{cav}_{ap}\}}_{y_s,\mathrm{TM}^z} = -\sqrt{\frac{j\omega\epsilon_{\{^{cav}_{ap}\}}\kappa_s}{\{^{g}_{a}\}\gamma^{\{^{cav}_{ap}\}}_{z_s}}}\cos\left(\frac{s\pi x}{\{^{g}_{a}\}}+\frac{s\pi}{2}\right) \tag{1c}$$

$$e^{\{^{cav}_{ap}\}}_{y_s,\mathrm{TE}^z} = -\sqrt{\frac{2j\omega\mu_{\{^{cav}_{ap}\}}}{\{^{g}_{a}\}\gamma^{\{^{cav}_{ap}\}}_{z_s}}}\sin\left(\frac{s\pi x}{\{^{g}_{a}\}}+\frac{s\pi}{2}\right) \tag{1d}$$

$$h^{\{^{cav}_{ap}\}}_{x_s,\mathrm{TE}^z} = \sqrt{\frac{2\gamma^{\{^{cav}_{ap}\}}_{z_s}}{j\omega\mu_{\{^{cav}_{ap}\}}\{^{g}_{a}\}}}\sin\left(\frac{s\pi x}{\{^{g}_{a}\}}+\frac{s\pi}{2}\right) \tag{1e}$$

$$h^{\{^{cav}_{ap}\}}_{z_s,\mathrm{TE}^z} = \frac{s\pi}{\{^{g}_{a}\}}\sqrt{\frac{2}{j\omega\mu_{\{^{cav}_{ap}\}}\{^{g}_{a}\}\gamma^{\{^{cav}_{ap}\}}_{z_s}}}\cos\left(\frac{s\pi x}{\{^{g}_{a}\}}+\frac{s\pi}{2}\right) \tag{1f}$$

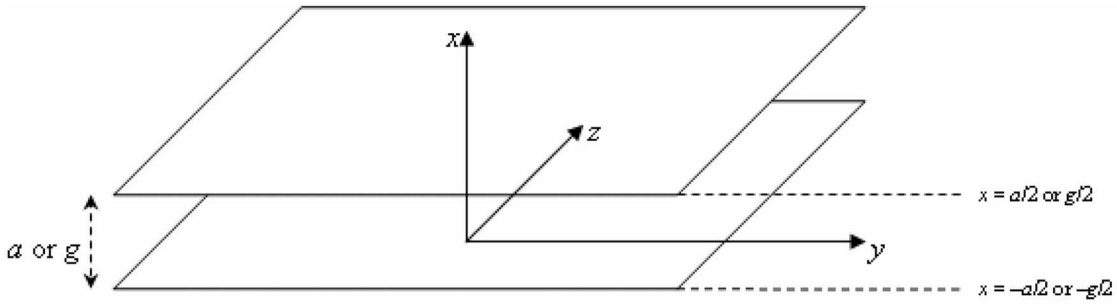

Figure 2. Parallel-plate waveguide with plate-separation a or g along x, for aperture or groove.

$$E_y^{\mathrm{TM}^z} = H_x^{\mathrm{TM}^z} = H_z^{\mathrm{TM}^z} = E_x^{\mathrm{TE}^z} = E_z^{\mathrm{TE}^z} = H_y^{\mathrm{TE}^z} = 0 \qquad (1g)$$

where $\kappa_s = \begin{cases} 1, & \text{when } s = 0 \\ 2, & \text{otherwise} \end{cases}$ and

$$\gamma_{z_s}^{\left\{{cav \atop ap}\right\}} = \sqrt{\left(\frac{s\pi}{\left\{{g \atop a}\right\}}\right)^2 - \omega^2 \mu_{\left\{{cav \atop ap}\right\}} \epsilon_{\left\{{cav \atop ap}\right\}}}$$

and whereby the upper and lower cases in the curly braces {} throughout these equations correspond to one another. The symbol g or a represents the width of either the groove (cavity) or aperture (iris) region, respectively, as also labeled by upper case "*cav*" and lower case "*ap*" in the curly braces, as will be explained later below. The integer s denotes the modal index of either the groove or aperture region, representing the number of half-cycle variation of the fields along the x direction.

[12] By these preceding equations, the PPW modes are orthonormalized, i.e.

$$\int_{x=0}^{a} \left[e_{x_{p,\mathrm{Tr}^z}}^{\left\{{cav \atop ap}\right\}}(x) h_{y_{u,\mathrm{Tw}^z}}^{\left\{{cav \atop ap}\right\}}(x) - e_{y_{p,\mathrm{Tr}^z}}^{\left\{{cav \atop ap}\right\}}(x) h_{x_{u,\mathrm{Tw}^z}}^{\left\{{cav \atop ap}\right\}}(x) \right] dx = \delta_{pr,uw}$$

$$\delta_{pr,uw} = \begin{cases} 1, \text{only when } pr \equiv uw, \text{i.e. } p = u, \mathrm{Tr}^z \equiv \mathrm{Tw}^z \langle = \mathrm{TE}^z \text{ or } \mathrm{TM}^z \rangle \\ 0, \qquad \text{otherwise} \end{cases}$$

as required for the derivation as well as utility of the PPW cavity Green's functions.

2.2. Expansion of Infinitely Long PEC-Equivalent Magnetic Aperture Strip Current Into PPW Modal Basis Functions

[13] Upon invocation of PEC equivalence, the grooves of the corrugations are filled up with PEC and the iris is replaced with an equivalent magnetic strip current of infinite expanse along the y-direction, expressed as:

$$\vec{M}^+(x) = \vec{E}_{ap}(x, z = 0^+) \times \hat{z} = \\ = e^{-jk_{y0}y} \left\{ \hat{x} \sum_{p_{\mathrm{TE}}} A_{p_{\mathrm{TE}}} e_{y_{p_{\mathrm{TE}}}}^{ap}(x) + \hat{y} \sum_{p_{\mathrm{TM}}} A_{p_{\mathrm{TM}}} \left[-e_{x_{p_{\mathrm{TM}}}}^{ap}(x) \right] \right\} \quad (2)$$

[14] It is highlighted that this magnetic current exists over the aperture only. Also note the vital term $e^{-jk_{y0}y}$ which is pertinent to the anticipated treatment of plane wave scattering by the corrugations later, i.e., they are illuminated by an incident plane wave with a forcing wave number k_{y0} along y defining the dominant Floquet harmonic. It is crucial to note that in the present formulation of the PPW modes, this $e^{-jk_{y0}y}$ must be universally present throughout. Since $+\hat{z}$ is used as the unit normal, pointing upwards into the upper half-space, hence this $\vec{M}^+$ is perceived positive just over $z = 0$ aperture, i.e., at $z = 0^+$, just outside the virtual PPW cavity (infinitely long along y). Correspondingly, the M just within the PPW cavity at $z = 0^-$ is: $\vec{M}^-(x) = -\vec{M}^+(x)$.

2.3. Radiated H-Field Into Grooves via PPW Cavity Green's Function

[15] Figure 3 shows the groove region of the T-shaped corrugations modeled as a shorted parallel-plate waveguide cavity, with "propagation" direction along z being perpendicular to the two infinitely long (along y) metallic plate-walls (parallel to xy plane, i.e., cross-sectional with respect to the propagation z-direction) serving as the shorting walls, at $z = -h$ and 0. On one of these two "end walls" (the one at

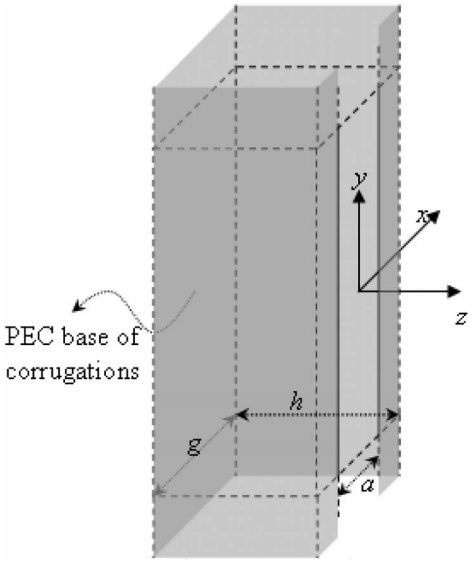

Figure 3. Groove region of corrugations modeled as a shorted parallel-plate waveguide cavity.

$z = 0$) locates an infinitely long (along y) magnetic strip current aperture, which may generally be smaller than the cross-sectional shorting metallic strip-wall, so as to model an iris.

[16] The full derivation of the PPW cavity Green's function would be too voluminous and thus cannot be provided in this paper. But as far as this work is concerned, for the magnetic source located at the $z = 0$ end of the PPW cavity, and for H-field observation also at that $z = 0$ end of the cavity, just to the left of the source, i.e., at 0^-, the observed transverse xy component of the H-field is directly written as:

$$\vec{H}_t^{z_s=z_2}(x_o, z_o = 0^-) = e^{-jk_{y0}y_o} \times \left[\begin{array}{l} -\sum_{p_{\mathrm{TM}}=0}^{\mathrm{P}_{\mathrm{TM}}^{cav}} \coth\left(\gamma_{z_{p_{\mathrm{TM}}}}^{cav} h\right) \vec{h}_{t_{p_{\mathrm{TM}}}}^{cav}(x_o) \sum_{u_{\mathrm{TM}}=0}^{U_{\mathrm{TM}}^{ap}-1} A_{u_{\mathrm{TM}}} \int_{x_s=-a/2}^{a/2} e_{x_{u_{\mathrm{TM}}}}^{ap}(x_s) h_{y_{p_{\mathrm{TM}}}}^{cav}(x_s) dx_s \\ \cdots + \sum_{p_{\mathrm{TE}}=1}^{\mathrm{P}_{\mathrm{TE}}^{cav}} \coth\left(\gamma_{z_{p_{\mathrm{TE}}}}^{cav} h\right) \vec{h}_{t_{p_{\mathrm{TE}}}}^{cav}(x_o) \sum_{u_{\mathrm{TE}}=1}^{U_{\mathrm{TE}}^{ap}} A_{u_{\mathrm{TE}}} \int_{x_s=-a/2}^{a/2} e_{y_{u_{\mathrm{TE}}}}^{ap}(x_s) h_{x_{p_{\mathrm{TE}}}}^{cav}(x_s) dx_s \end{array} \right] \tag{3}$$

where $\vec{h}_{t_{p_{\mathrm{TE}}}}^{cav} = \hat{x} h_{x_{p_{\mathrm{TE}}}}^{cav} + \hat{y} h_{y_{p_{\mathrm{TE}}}}^{cav}$, with $\Psi = M$ or E. The o and s subscripts of x denote the observation and source coordinates. U_{TM}^{ap} and U_{TE}^{ap} are the truncated numbers of TM and TE type PPW-cavity modes considered for the aperture fields.

2.4. Fourier Transform of PEC-Equivalent Magnetic Strip-Current Over Iris-Type Aperture

[17] The magnetic current of (2) may be restated as

$$\tilde{M}_{\left\{\begin{smallmatrix} x \\ y \end{smallmatrix}\right\}}(x_s, z_s = 0^+) = \sum_{u_{\left\{\begin{smallmatrix} \mathrm{TE} \\ \mathrm{TM} \end{smallmatrix}\right\}}=\left\{\begin{smallmatrix} 1 \\ 0 \end{smallmatrix}\right\}}^{U^{ap}_{\left\{\begin{smallmatrix} \mathrm{TE} \\ \mathrm{TM} \end{smallmatrix}\right\}}} A_{u,\left\{\begin{smallmatrix} \mathrm{TE} \\ \mathrm{TM} \end{smallmatrix}\right\}} \tilde{m}_{\left\{\begin{smallmatrix} x \\ y \end{smallmatrix}\right\}_{u,\left\{\begin{smallmatrix} \mathrm{TE} \\ \mathrm{TM} \end{smallmatrix}\right\}}} \left(x_s, k_{y_{n=0}}\right) \tag{4a}$$

$$\tilde{m}_{\left\{\begin{smallmatrix} x \\ y \end{smallmatrix}\right\}_{u,\left\{\begin{smallmatrix} \mathrm{TE} \\ \mathrm{TM} \end{smallmatrix}\right\}}} \left(x_s, k_{y_{n=0}}\right) = \pm e^{ap}_{\left\{\begin{smallmatrix} y \\ x \end{smallmatrix}\right\}_{u,\left\{\begin{smallmatrix} \mathrm{TE} \\ \mathrm{TM} \end{smallmatrix}\right\}}} (x_s) \tag{4b}$$

where the single tilde signifies that these are already in the k_y spectral domain, evaluated at a single $k_{yn=0} = k \sin\theta_0 \sin\phi_0$, in which θ_0 and ϕ_0 are the incident angles of the impingent plane wave (defining the dominant Floquet harmonic) that illuminates the corrugations from above, and k is the wave number of the medium above the corrugations from which the excitation plane wave arrives (emerges).

[18] Transforming these into spectral ($k_{x\zeta}$, $k_{yn=0} = k_y^{ex}$) domain [involving just a single (line/contour) integration with respect to x_s], we write:

$$\tilde{\tilde{M}}_{\left\{\begin{smallmatrix} x \\ y \end{smallmatrix}\right\}}\left(k_{x_\zeta}, k_{y_{n=0}}, z_s = 0^+\right) = \sum_{u_{\left\{\begin{smallmatrix} \mathrm{TE} \\ \mathrm{TM} \end{smallmatrix}\right\}}=\left\{\begin{smallmatrix} 1 \\ 0 \end{smallmatrix}\right\}}^{U^{ap}_{\left\{\begin{smallmatrix} \mathrm{TE} \\ \mathrm{TM} \end{smallmatrix}\right\}}} A_{u,\left\{\begin{smallmatrix} \mathrm{TE} \\ \mathrm{TM} \end{smallmatrix}\right\}} \tilde{\tilde{m}}_{\left\{\begin{smallmatrix} x \\ y \end{smallmatrix}\right\}_{u,\left\{\begin{smallmatrix} \mathrm{TE} \\ \mathrm{TM} \end{smallmatrix}\right\}}} \left(k_{x_\zeta}, k_{y_{n=0}}\right) \tag{5a}$$

$$\tilde{\tilde{m}}_{\left\{\begin{smallmatrix} x \\ y \end{smallmatrix}\right\}_{u,\left\{\begin{smallmatrix} \mathrm{TE} \\ \mathrm{TM} \end{smallmatrix}\right\}}} \left(k_{x_\zeta}, k_{y_{n=0}}\right) = \int_{x_s=-\frac{a}{2}}^{x_s=+\frac{a}{2}} \tilde{m}_{\left\{\begin{smallmatrix} x \\ y \end{smallmatrix}\right\}_{u,\left\{\begin{smallmatrix} \mathrm{TE} \\ \mathrm{TM} \end{smallmatrix}\right\}}} \left(x_s, k_{y_{n=0}}\right) e^{+jk_{x_\zeta} x_s} dx_s \tag{5b}$$

with

$$k_{x_\zeta} = k_0 \sin\theta_0 \cos\phi_0 + 2\zeta\pi/d_x, \tag{5c}$$

such that the inverse transform from spectral k_x to spatial x domain only requires a summation over discrete spectral components defined by this (5c) due to the periodicity along only x (but not y) with period d_x. The ζ is an integer denoting the Floquet harmonic index, which we have intently used instead of m that would had been in harmony with the $n = 0$ of k_y but so as not to confuse with the magnetic basis currents $\tilde{m}$ and $\tilde{\tilde{m}}$. Symbols θ_0 and ϕ_0 are the angular coordinates defining the direction of the dominant Floquet modal beam, defined simply by the incidence angles of the impingent plane wave (the primary excitation of the corrugations), and k_0 is the usual freespace wave number.

2.5. Spectral Magnetic Fields Radiated by Spectral Basis Magnetic Currents Located on Surface of Infinite PEC Ground Plane

[19] The spectral basis currents of this (5b) are subsequently employed as the secondary sources for the scattering scenario (as opposed to the primary incident plane wave source for the excitation scenario), which is the excitation of the *uncorrugated* perfect electric conducting (PEC) planar structure, for which the grooves of the corrugations have been filled up with PEC (upon PEC equivalence). The spectral fields radiated by these spectral basis currents (placed just on the PEC surface) into the medium above the corrugations are obtained from a numerical spectral Green's function for treating multilayer structures known as G1DMULT [*Sipus et al.*, 1998; *Ng Mou Kehn et al.*, 2006], being the core routine of this technique, i.e.

$$\tilde{\tilde{H}}_w^{\tilde{\tilde{m}}_{[x,y]_{u,[\mathrm{TE,TM}]}}} = \tilde{\tilde{G}}_{H_w}^{M_{[x,y]}} \cdot \tilde{\tilde{m}}_{[x,y]_{u,[\mathrm{TE,TM}]}}, \tag{6}$$

where the w subscript may denote either x or y component of the radiated spectral H-field. The spectral dyadic Green's function G is characterized by superscript $M_{[x,y]}$ signifying the magnetic current source type and its x or y component of the secondary excitation source, whereas its subscript H_w indicates the type of the radiated field and its component. The driving spectral basis current is indicated as $\tilde{\tilde{m}}_{[x,y]_{u,[\mathrm{TE,TM}]}}$, which is from (5b), and is reminded that it pertains to a certain ζth Floquet harmonic being the $k_{x\zeta}$ spectral component of (5c). The complete details of this numerical spectral Green's function and its explicit expressions are also way too massive and thus are not provided here.

2.6. Spatial Fields Radiated by Entire Array of Magnetic Strip Currents Into Region Above Corrugations

[20] As explained earlier at (5c), the inverse transform of the spectral field of (6) is written as

$$\tilde{H}_w^{\tilde{m}_{[x,y]_{u,[\mathrm{TE,TM}]}}} = \frac{1}{d_x}\sum_{\zeta} \tilde{\tilde{H}}_{\zeta}^{\tilde{m}_{[x,y]_{u,[\mathrm{TE,TM}]}}} e^{-j\left(k_{x_\zeta}x + k_{y0}y\right)}, \tag{7}$$

[21] This (7) then constitutes the w-component of the *semi*-spatial-domain H-field radiated by the [x, y]-directed *semi*-spatial (in x only) domain (u,[TE,TM])th basis current $\tilde{m}_{[x,y]_{u,[\mathrm{TE,TM}]}}(x)$ of (4b). Remember that we are now always at a single component in the k_y spectral domain, being $k_y = k_{y0} = k_0\sin\theta\sin\phi$. Hence, a single tilde remains on the left-hand side of (7). Assuming an odd integer Z as the total truncated number of Floquet harmonics considered (for the purpose of practical computations), the summation typically runs from $\zeta = -(Z-1)/2$ to $(Z-1)/2$. In the computations of this paper, $Z = 49$ has been selected, which is sufficient to provide accurate results.

[22] Subsequently, the total fields radiated by all basis currents would just entail a summation over the basis indices, each term scaled by an amplitude coefficient, according to (4a), i.e.

$$\tilde{H}_w^{M_{[x,y]}} = \sum_{u_{[\mathrm{TE,TM}]}=[1,0]}^{U^{ap}_{[\mathrm{TE,TM}]}} A_{u,[\mathrm{TE,TM}]}\tilde{H}_w^{\tilde{m}_{[x,y]_{u,[\mathrm{TE,TM}]}}} \tag{8}$$

[23] This represents the w-component of the *semi*-spatial-domain H-field radiated by the [x, y]-directed magnetic current scatterer source components. It is noted that this remains only the scattered magnetic fields. The known fields due to the primary excitation source radiating in the bare uncorrugated infinite PEC ground environment and observed at the PEC surface where the equivalent magnetic current strips are located are also obtained from G1DMULT, but shall just directly be stated as $H_w^{prim\,excit}$ without further specification.

2.7. Boundary Conditions: Continuity of Tangential H-Fields Across PPW Cavity Aperture

[24] The boundary condition enforcing the continuity of the tangential magnetic fields across the iris-type aperture of the parallel-plate waveguide cavity is stated as:

$$\vec{H}_t^{z_s=z_2}(x_o, z_o = 0^-) = \begin{bmatrix} \hat{x}H_x^{M_{x+y}} \\ \hat{y}H_y^{M_{x+y}} \end{bmatrix} + \begin{bmatrix} \hat{x}H_x^{prim\,excit} \\ \hat{y}H_y^{prim\,excit} \end{bmatrix} \tag{9}$$

where $H_w^{M_{x+y}} = H_w^{M_x}\left(\vec{r}_o \in A_{ap}\right) + H_w^{M_y}\left(\vec{r}_o \in A_{ap}\right)$, in which $\vec{r}_o$ represents the position vector of the observation coordinates, which span over the aperture symbolized as A_{ap}. As before, w may be x or y.

2.8. Galerkin Weighting and Construction of Intermediate Matrices

[25] Taking $\int_{x_o=-\frac{a}{2}}^{x_o=\frac{a}{2}} \left[\vec{e}^{ap}_{t_{\mathrm{TM}}}(x_o) \times \_\_ \cdot \hat{z}\right]$ throughout the boundary condition (9), for $v = 1, 2, \ldots, U^{ap}_{\Phi}$ (where Φ may denote TE or TM), a total number of equations that equals the number of unknown coefficients of the basis functions expanding the aperture magnetic currents are generated. This system of equation can be cast into a matrix equation. The intermediate matrices that build up to this matrix equation are as follow. The left-hand side square-bracketed quantities are the matrices while the right-hand side ones are the expressions of their (p, q) th elements, where p and q are the row and column indices, and as identified by the index-labelers in round-brackets alongside the left-hand side matrices.

$$[A_w^{\mathrm{T}\Psi}(\zeta, u_{\mathrm{T}\Psi})]_{Z\times U^{ap}_{\mathrm{T}\Psi}} = \frac{1}{d_x}\tilde{\tilde{H}}_w^{\tilde{m}_{[x,y]_{u,[\mathrm{TE,TM}]}}} \tag{10}$$

for $w = x$ or y, $\Psi = E$ or M, independently.

$$\left[B^{\{\mathrm{TM,TE}\}}_{\{x,y\}}\left(v_{\{\mathrm{TM,TE}\}},\zeta\right)\right]_{U^{ap}_{\{\mathrm{TM,TE}\}}\times Z} = \int_{x_o=-\frac{a}{2}}^{x_o=\frac{a}{2}} e^{ap}_{\{x,y\}_{v_{\{\mathrm{TM,TE}\}}}}(x_o)e^{-jk_{x_\zeta}x_o}dx_o \tag{11}$$

$$\left[C_{\{\mathrm{TM,TE}\}}\left(u_{\{\mathrm{TM,TE}\}},p_{\{\mathrm{TM,TE}\}}\right)\right]_{U^{ap}_{\{\mathrm{TM,TE}\}}\times \mathrm{P}^{cav}_{\{\mathrm{TM,TE}\}}} = \int_{x_s=-a/2}^{a/2} e^{ap}_{\{x,y\}_{u_{\{\mathrm{TM,TE}\}}}} \cdot (x_s)h^{cav}_{\{y,x\}_{p_{\{\mathrm{TM,TE}\}}}}(x_s)dx_s \tag{12}$$

[26] Next, the matrix $\Phi(p_{\mathrm{T}\Psi}, p_{\mathrm{T}\Psi})$ is defined, which is a diagonal matrix whose diagonal elements are $\coth(\gamma^{cav}_{z_{p=1}}h)$, $\coth(\gamma^{cav}_{z_{p=2}}h)$, …, $\coth(\gamma^{cav}_{z_{p=P_{\mathrm{T}\zeta}}}h)$, for $\Psi = E$ and M.

$$\left[V_{\left\{\begin{smallmatrix}\mathrm{TE}\\ \mathrm{TM}\end{smallmatrix}\right\}}\left(v_{\left\{\begin{smallmatrix}\mathrm{TE}\\ \mathrm{TM}\end{smallmatrix}\right\}},1\right)\right]_{U^{ap}_{\left\{\begin{smallmatrix}\mathrm{TE}\\ \mathrm{TM}\end{smallmatrix}\right\}}\times 1} = \pm H^{prim\,excit}_{\left\{\begin{smallmatrix}x\\ y\end{smallmatrix}\right\}} \int_{x_o=-\frac{a}{2}}^{x_o=\frac{a}{2}} e^{ap}_{\left\{\begin{smallmatrix}y\\ x\end{smallmatrix}\right\}_v\left\{\begin{smallmatrix}\mathrm{TE}\\ \mathrm{TM}\end{smallmatrix}\right\}}(x_o)e^{-j\overbrace{k_{x_{\zeta=0}}}^{k_x^{ex}}x_o}dx_o$$

$$\left[V_{final}(v,1)\right]_{(U^{ap}_{\mathrm{TM}}+U^{ap}_{\mathrm{TE}})\times 1} = \left\{\begin{matrix}[V_{\mathrm{TM}}(v_{\mathrm{TM}},1)]_{U^{ap}_{\mathrm{TM}}\times 1}\\ [V_{\mathrm{TE}}(v_{\mathrm{TE}},1)]_{U^{ap}_{\mathrm{TE}}\times 1}\end{matrix}\right\} \tag{13}$$

2.9. Matrix Operations and Construction of Ultimate Moment-Method Matrix Equation

[27] With the foregoing intermediate matrices laid out, the following matrix operations are then performed.

$$\begin{aligned}[M_{11}(v_{\mathrm{TM}},u_{\mathrm{TM}})]_{U^{ap}_{\mathrm{TM}}\times U^{ap}_{\mathrm{TM}}} = {} & \left[B_x^{\mathrm{TM}}(v_{\mathrm{TM}},\zeta)\right]_{U^{ap}_{\mathrm{TM}}\times Z}\left[A_y^{\mathrm{TM}}(\zeta,u_{\mathrm{TM}})\right]_{Z\times U^{ap}_{\mathrm{TM}}} \\ & + \cdots + \left\{[C_{\mathrm{TM}}(v_{\mathrm{TM}},p_{\mathrm{TM}})]_{U^{ap}_{\mathrm{TM}}\times \mathrm{P}^{cav}_{\mathrm{TM}}} \right. \\ & \left. \cdot\,[\Phi(p_{\mathrm{TM}},p_{\mathrm{TM}})]_{\mathrm{P}^{cav}_{\mathrm{TM}}\times \mathrm{P}^{cav}_{\mathrm{TM}}}\right\}_{U^{ap}_{\mathrm{TM}}\times \mathrm{P}^{cav}_{\mathrm{TM}}} \\ & \cdot\left[\left\{[C_{\mathrm{TM}}(u_{\mathrm{TM}},p_{\mathrm{TM}})]_{U^{ap}_{\mathrm{TM}}\times \mathrm{P}^{cav}_{\mathrm{TM}}}\right\}^{\mathrm{T}}\right]_{\mathrm{P}^{cav}_{\mathrm{TM}}\times U^{ap}_{\mathrm{TM}}}\end{aligned} \tag{14}$$

$$[M_{12}(v_{\mathrm{TM}},u_{\mathrm{TE}})]_{U^{ap}_{\mathrm{TM}}\times U^{ap}_{\mathrm{TE}}} = \left[B_x^{\mathrm{TM}}(v_{\mathrm{TM}},\zeta)\right]_{U^{ap}_{\mathrm{TM}}\times Z}\left[A_y^{\mathrm{TE}}(\zeta,u_{\mathrm{TE}})\right]_{Z\times U^{ap}_{\mathrm{TE}}} \tag{15}$$

$$[M_{21}(v_{\mathrm{TE}},u_{\mathrm{TM}})]_{U^{ap}_{\mathrm{TE}}\times U^{ap}_{\mathrm{TM}}} = -\left[B_y^{\mathrm{TE}}(v_{\mathrm{TE}},\zeta)\right]_{U^{ap}_{\mathrm{TE}}\times Z}\left[A_x^{\mathrm{TM}}\left(\zeta,u_{\mathrm{TM}}\right)\right]_{Z\times U^{ap}_{\mathrm{TM}}} \tag{16}$$

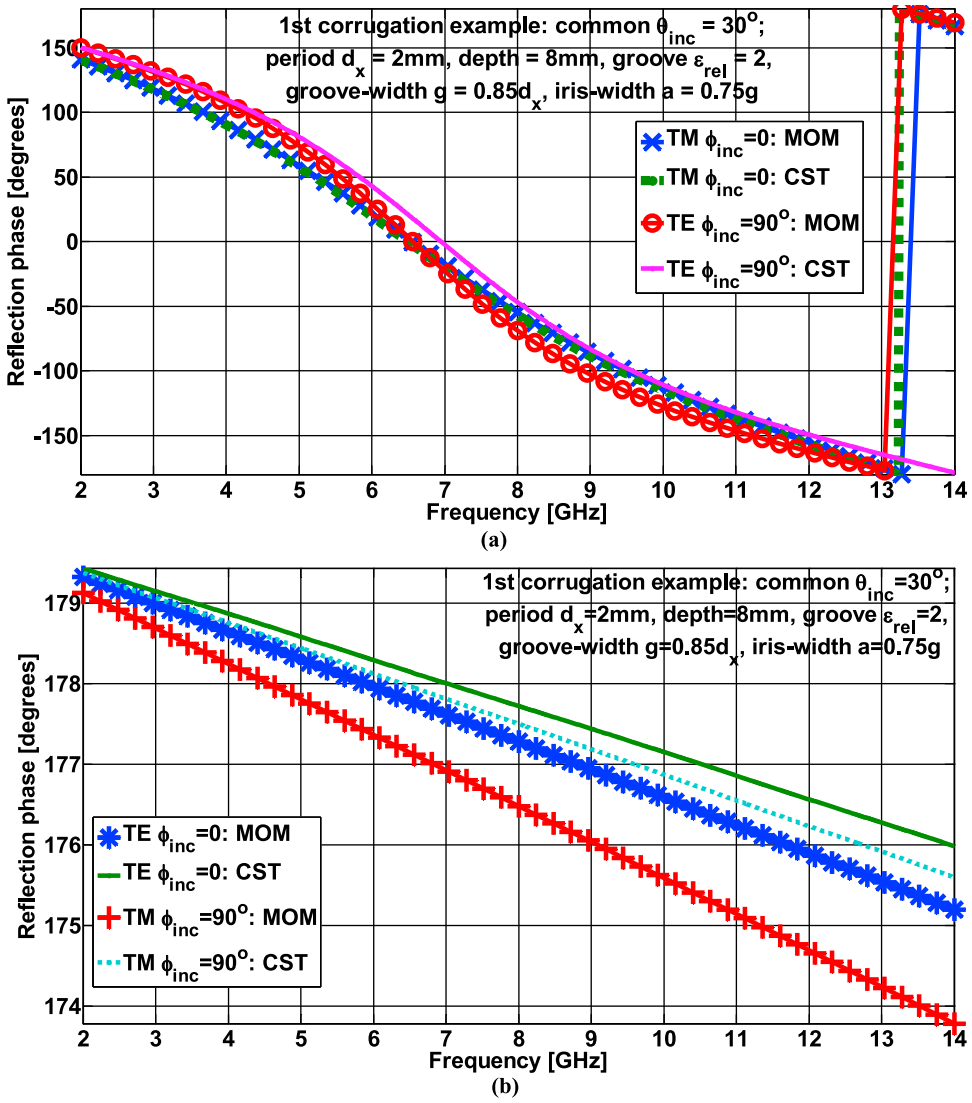

Figure 4. Comparisons between reflection-phase diagrams generated by present moment-method (MOM) and CST for first arbitrary example with common $\theta_{inc} = 30°$, for (a) TM polarization $\phi_{inc} = 0$ and TE polarization $\phi_{inc} = 90°$ and (b) TM polarization $\phi_{inc} = 90°$ and TE polarization $\phi_{inc} = 0$.

$$
\begin{aligned}
[M_{22}(v_{\mathrm{TE}},u_{\mathrm{TE}})]_{U_{\mathrm{TE}}^{ap}\times U_{\mathrm{TE}}^{ap}} &= -\left[B_y^{\mathrm{TE}}(v_{\mathrm{TE}},\zeta)\right]_{U_{\mathrm{TE}}^{ap}\times Z}\left[A_x^{\mathrm{TE}}(\zeta,u_{\mathrm{TE}})\right]_{Z\times U_{\mathrm{TE}}^{ap}} \\
&\quad + \cdots\cdots + \left\{[C_{\mathrm{TE}}(v_{\mathrm{TE}},p_{\mathrm{TE}})]_{U_{\mathrm{TE}}^{ap}\times \mathrm{P}_{\mathrm{TE}}^{cav}}\right. \\
&\quad \left.\cdot\,[\Phi(p_{\mathrm{TE}},p_{\mathrm{TE}})]_{\mathrm{P}_{\mathrm{TE}}^{cav}\times\mathrm{P}_{\mathrm{TE}}^{cav}}\right\}_{U_{\mathrm{TE}}^{ap}\times \mathrm{P}_{\mathrm{TE}}^{cav}} \\
&\quad \cdot\left[\left\{[C_{\mathrm{TE}}(u_{\mathrm{TE}},p_{\mathrm{TE}})]_{U_{\mathrm{TE}}^{ap}\times\mathrm{P}_{\mathrm{TE}}^{cav}}\right\}^{\mathrm{T}}\right]_{\mathrm{P}_{\mathrm{TE}}^{cav}\times U_{\mathrm{TE}}^{ap}}
\end{aligned}
\tag{17}
$$

[28] These submatrices are then cascaded to form the final matrix:

$$
[M_{final}]_{(U_{\mathrm{TM}}^{ap}+U_{\mathrm{TE}}^{ap})\times(U_{\mathrm{TM}}^{ap}+U_{\mathrm{TE}}^{ap})} = \begin{Bmatrix} [M_{11}(v_{\mathrm{TM}},u_{\mathrm{TM}})]_{U_{\mathrm{TM}}^{ap}\times U_{\mathrm{TM}}^{ap}} & [M_{12}(v_{\mathrm{TM}},u_{\mathrm{TE}})]_{U_{\mathrm{TM}}^{ap}\times U_{\mathrm{TE}}^{ap}} \\ [M_{21}(v_{\mathrm{TE}},u_{\mathrm{TM}})]_{U_{\mathrm{TE}}^{ap}\times U_{\mathrm{TM}}^{ap}} & [M_{22}(v_{\mathrm{TE}},u_{\mathrm{TE}})]_{U_{\mathrm{TE}}^{ap}\times U_{\mathrm{TE}}^{ap}} \end{Bmatrix} \tag{18}
$$

[29] Finally, the ultimate matrix equation is stated as:

$$
[M_{final}]_{(U_{\mathrm{TM}}^{ap}+U_{\mathrm{TE}}^{ap})\times(U_{\mathrm{TM}}^{ap}+U_{\mathrm{TE}}^{ap})}\left\{\begin{bmatrix} A_{u_{\mathrm{TM}}=0} \\ \vdots \\ A_{u_{\mathrm{TM}}=U_{\mathrm{TM}}^{ap}} \end{bmatrix}\begin{bmatrix} A_{u_{\mathrm{TE}}=1} \\ \vdots \\ A_{u_{\mathrm{TE}}=U_{\mathrm{TE}}^{ap}} \end{bmatrix}\right\}_{(U_{\mathrm{TM}}^{ap}+U_{\mathrm{TE}}^{ap})\times 1} = [V_{final}(v,1)]_{(U_{\mathrm{TM}}^{ap}+U_{\mathrm{TE}}^{ap})\times 1} \tag{19}
$$

which can then be solved for the vector containing the unknown coefficients via matrix inversion.

3. Numerical Results: Validation With CST

[30] Two groups of numerical results computed by the entirely self-developed numerical code based on the present formulation are now presented: (A) reflection phase

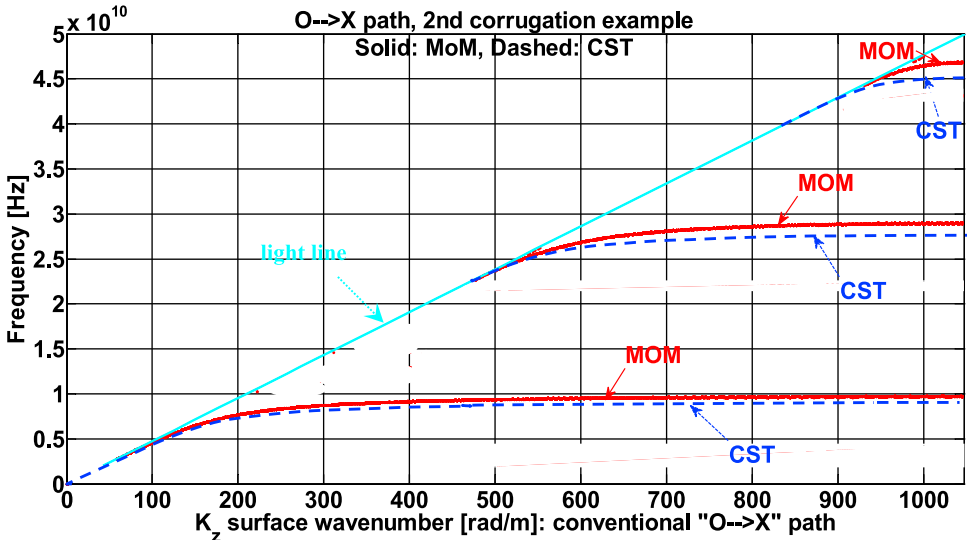

Figure 5a. Dispersion diagram (O → X path) of second arbitrary example. Solid lines: present moment-method, dashed lines: CST. The light-line is as shown.

diagrams, and (B) dispersion diagrams. These results shall be compared with those generated by a commercial full-wave simulator: CST Microwave Studio®.

3.1. Reflection-Phase Diagrams

[31] The parameters of an arbitrary example of corrugations for validation are as follow, according to Figure 1: period d_x = 2 mm, depth h = 8 mm, relative permittivity and permeability of the filling, ϵ_{cav} = 2 and μ_{cav} = 1, groove-width $g = 0.85d_x$, and aperture-width $a = 0.75g$. The following graphs of Figure 4 show the plots of the reflection phase against the frequency, for both polarizations (TM^z and TE^z) and in the two principal incidence planes (ϕ_{inc} = 0 and 90°), for a certain theta-angle: θ_{inc} = 30°, generated by the two numerical tools: the code based on the present moment method, and the full-wave simulator CST. Evidently, the agreement between the two approaches is very good.

[32] As observed, when the polarization of the incident plane wave (orientation of the incident E-field) is parallel to the metallic corrugations, the reflection phase is close to 180° at all investigated frequencies, which is as expected.

3.2. Dispersion Diagrams

[33] Another arbitrarily selected corrugation example shall be considered for the validation, this time in terms of the dispersion diagram. The parameters of this second example are stated as follow: d_x = 3 mm, h = 4 mm, ε_{cav} = 3 and μ_{cav} = 1, $g = 0.55d_x$, and $a = 0.45g$. The comparison of its dispersion diagram generated by the present moment method code with that simulated by CST is conveyed by Figures 5a and 5b, in which the characterization of the surface-wave

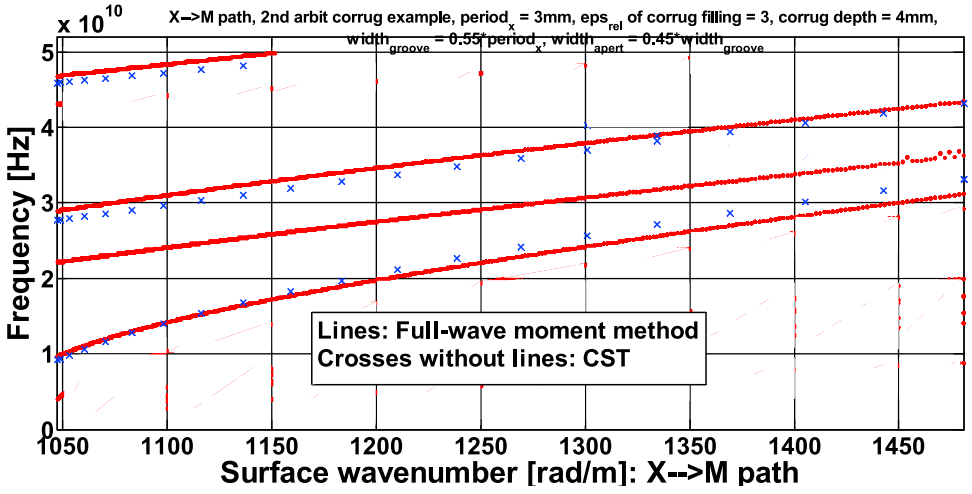

Figure 5b. Dispersion diagram (X → M path) of second arbitrary example. Solid lines: present moment-method, crosses without lines: CST.

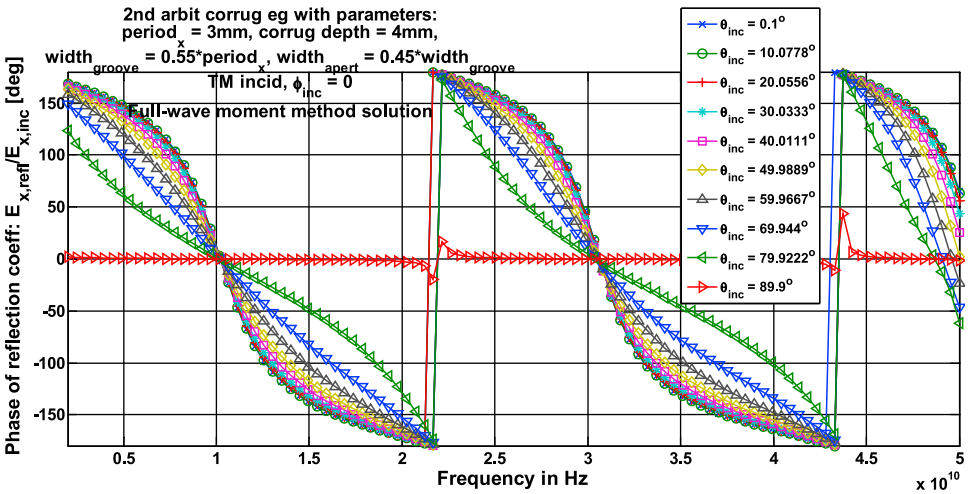

Figure 6. Reflection phase diagram for second arbitrary example, TM^z polarization, $\phi_{inc} = 0$, *various* θ_{inc} ranging from 0 to 90°.

modal propagation along the principal x-direction perpendicular to the corrugations up till the Brillouin limit (Bragg condition: $k_x = \pi/d_x$) is shown in Figure 5a whereas that along an oblique direction with a fixed surface modal wave number component of $k_x = \pi/d_x$ but varying k_y (increasing from zero) is given by Figure 5b, of which the horizontal axis quantity $k_{surf} = \sqrt{(\pi/d_x)^2 + k_y^2}$ varies from π/d_x to $\sqrt{2}\pi/d_x$. The former graph is formally termed as the OX path whereas the latter as the XM path of the irreducible Brillouin zone. Once again, the correctness and accuracy of the present formulation is validated and verified, for both the principal as well as oblique directions of surface wave modal propagation.

[34] An interesting aspect is now pointed out. The frequencies at which the dispersion traces approach zero slope coincide perfectly with the so-called "soft" frequencies [*Kildal*, 1990] of the corrugations, defined as

$$f_n^{soft} = c(2n+1)/\left(4d_{soft}\sqrt{\varepsilon_{rel,cav}}\right) \tag{20}$$

where n is an integer representing the order of the soft boundary condition, c is the speed of light in vacuum, d_{soft} is the depth of the corrugations at which the soft boundary condition holds, being simply the groove depth d, and $\varepsilon_{rel,cav}$ is the relative permittivity of the dielectric filling the grooves. These frequencies thus provide the upper-edge of each surface-wave passband, which is also the lower-edge of each stopband. Remarkably, as will be apparent later by the established relationship between the reflection-phase and dispersion diagrams in section 4, these frequencies shall also be the AMC (or HIS) frequencies at which the reflection-phase is zero, i.e., $f_n^{soft} = f_n^{AMC}$, where n is that same order.

4. Relations Between O → X Dispersion Diagrams and Reflection-Phase Diagrams for TM^z-Polarized Incidence in Plane Perpendicular to Corrugations

[35] Remarkable observations shall now be made in this section. Consider the following $E_{x,refl}/E_{x,inc}$ reflection-phase diagram in Figure 6 for the second arbitrary example, for TM^z polarized incidence, $\phi_{inc} = 0$ for various θ_{inc} angles ranging from zero (normal incidence) to 90 degrees (grazing incidence). For the first two AMC frequencies at which the corrugations exhibit high-impedance surface (or AMC) properties (reflection phase = 0) are all almost the same regardless of the theta angles of incidence. In addition, the frequencies at which they display low-impedance surface (or AEC) properties (reflection phase = 180 deg) are also the same for all theta angles. And upon shrewd scrutiny of its associated dispersion diagram in Figure 5a, it is discovered that the frequency ranges over which the phase angles are positive in the reflection phase diagram represent surface-wave passbands in the dispersion diagram whereas the bands of negative phase values define surface-wave stopbands in the dispersion diagram. Explained in detail, the band from 0 to around 10 GHz corresponding to reflection-phase from +180 deg to 0 (first AMC condition occurs) observed in Figure 6 concurs with the passband of the dominant surface wave mode also seen to exist from 0 to around 10 GHz in Figure 5a. Following this, the range from the latter 10 GHz to around 22 GHz pertaining to reflection-phase of 0 to −180 deg is seen to fit nicely with the first stopband of surface waves observed in Figure 5a. Next, the band from this latter 22 GHz to around 30.5 GHz corresponding to reflection-phase of +180 deg to 0 again matches well with the second passband in Figure 5a. Likewise, the 30.5 GHz to 43 GHz range with negative reflection-phases (0 to −180 deg) in Figure 6 shows up as the second stopband in Figure 5a. Finally, the range of 43 to about 48 GHz with positive reflection-phases (+180 deg to 0) characterizes the last passband of Figure 5a.

5. Transverse Resonance Technique (TRT)

[36] The characteristic equations of the planar TM corrugated structure for both principal (perpendicular to the ridges) and oblique directions of surface propagation can be derived using the transverse resonance technique (TRT), solving of which enables the generation of the dispersion diagram. This entails matching of the impedances at the $z =$

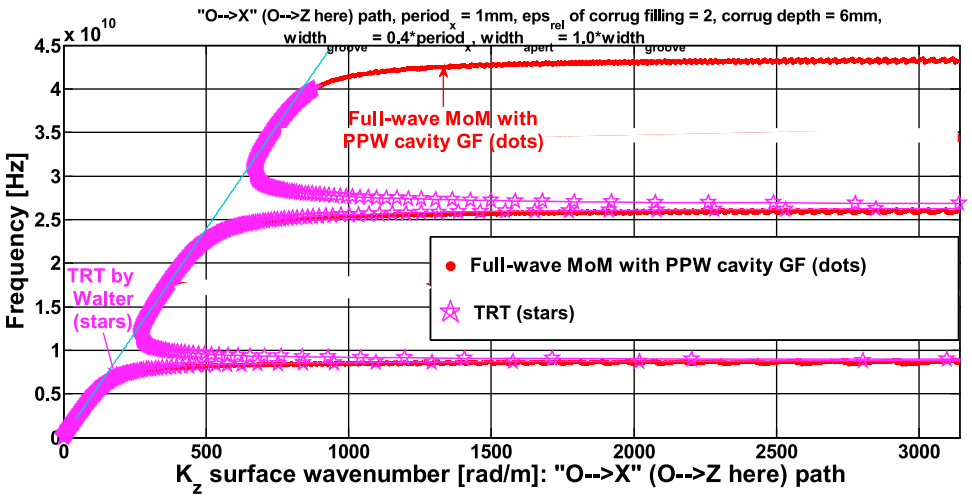

Figure 7. Dispersion diagram of O → X path for $g = 0.4d_x$ generated by full-wave moment method and TRT, for $d_x = 1$ mm, $\epsilon_{rel,cav} = \epsilon_{cav}/\epsilon_0 = 2$, $h = 6$ mm.

0 interface (Figure 1) separating the corrugations (grooves and ridges) from the upper half-space and is based on the assumption that only the propagating TM mode exists in the upper half-space and that the field in the corrugated region ($-h < z < 0$) is in the form of a TEM wave in a shorted parallel-plate region. Mathematically,

$$\frac{k_z}{\omega\varepsilon_0} + j\frac{g}{d_x}\sqrt{\frac{\mu_{cav}}{\varepsilon_{cav}}}\tan\left(\omega\sqrt{\mu_g\varepsilon_g}h\right) = 0 \tag{21a}$$

where g/d_x is an incorporated correction factor that accounts for the average impedance, and $k_z = \sqrt{(2\pi f)^2\mu_0\varepsilon_0 - k_x^2}$ with $k_y = 0$ for surface-wave propagation direction that is perpendicular to the corrugations. This then yields

$$k_x = \sqrt{4(\pi f)^2\mu_0\varepsilon_0 + 4\mu_0\varepsilon_0\left(\frac{g\pi f}{d_x}\right)^2\frac{\mu_{rel,cav}}{\epsilon_{rel,cav}}\tan^2\left(2\pi fh\sqrt{\mu_{cav}\varepsilon_{cav}}\right)} \tag{21b}$$

for the principal direction (O → X path). This (21b) may then be directly evaluated (solved) for the resonant k_x for the O → X propagation path.

[37] Figure 7 displays the band diagram for the principal surface-wave propagation direction of an arbitrarily selected case with the following parameters: $g/d_x = 0.4$, $d_x = 1$ mm, $\varepsilon_{rel,cav} = \varepsilon_{cav}/\varepsilon_0 = 2$, and $h = 6$ mm, generated using the full-wave moment method code and the TRT using (21b). The characteristic equation (21b) produces a dispersion trace which takes on the form of cyclic 'peaking' of the surface-wave propagation constant k_x (along the x-direction perpendicular to the corrugations) at various resonant frequencies. Moreover, the trace just 'grazes' the light-line, i.e., it is tangent to it, occurring at frequencies slightly above those whereby the trace has dropped back to its local minima and begun to rise again. However, as observed, only the rising parts of the 'peaking' trace after the 'grazing' are relevant, for which the agreement with the dispersion trace generated by the full-wave moment method code is seen to be superb. In fact, they agree so well that the traces are virtually indistinguishable.

[38] By equating the derivative of k_x in (21b) with respect to the frequency f to $2\pi/c$ (c being the speed of light in vacuum) and solving for f as the roots of the resultant equation, we can obtain the cutoff frequency of each surface-wave mode, or equivalently, the lower-edge frequency of each surface-wave passband, being also the upper-edge frequency of each stopband. Mathematically,

$$\frac{4\pi^2 f\mu_0\varepsilon_0}{k_x}\left\{1 + \frac{\mu_{rel,cav}}{\varepsilon_{rel,cav}}\left(\frac{g}{d_x}\right)^2\tan\left(2\pi fd\sqrt{\mu_{cav}\varepsilon_{cav}}\right)\cdot\left[\begin{array}{l}\tan\left(2\pi fd\sqrt{\mu_{cav}\varepsilon_{cav}}\right)\cdots \\ \cdots + 2\pi fd\sqrt{\mu_{cav}\varepsilon_{cav}}\sec^2\left(2\pi fd\sqrt{\mu_{cav}\varepsilon_{cav}}\right)\end{array}\right]\right\} - \frac{2\pi}{c} = 0 \tag{22}$$

[39] According to the relationship established in section 4, the frequency roots of this equation shall then also constitute the so-called AEC frequencies at which the reflection phase equals ±180°, regardless of the incidence θ_{inc} angle.

[40] Therefore, together with the f_n^{soft} of (20), the f roots of this (22) respectively provide both the AMC (HIS) and AEC (LIS) frequencies of planar corrugated surfaces, making them important mathematical quantities.

6. Closed-Form Expression for TM^z Reflection-Phase as Analytic Function of Parameters

[41] From the relationship struck in section 4 between the positivity and negativity of the reflection phase (for TM^z polarized incidence in the $\phi_{inc} = 0$ plane perpendicular to the corrugations) with the surface-wave passband and stopband (in the O → X dispersion diagram), respectively, it may be anticipated that the analytic expression of the surface-wave propagation constant of (21b) can be used to derive a likewise explicit closed-form formula for the reflection-phase in terms of the various corrugation parameters. The motivation behind this idea stems from the herein-discovered phenomenon that at least the behavioral connection (in the cyclical sense) between the propagation constant and the reflection-phase, when both are plotted against the frequency, has already been established, and thus the k_x expression of (21b) as a function of all parameters (except the incident theta

angle, which will be taken care of later) offers an excellent starting platform to build on.

[42] The thought process of the derivation shall now be described. First, concentrate on the graphs of the reflection-phase and surface-wave propagation constant versus frequency (simply, the reflection-phase and dispersion diagrams which we have been seeing in the preceding figures, but with the axes of the latter diagram swapped, i.e., the propagation constant is now represented by the vertical axis). It is observed that the rise of each modal propagation constant with frequency gets increasing steep as the surface-wave enters deeper into the slow-wave region. This is corresponded with the increasing steep fall of the reflection-phase with frequency from 180°. As the slope of the propagation-constant versus frequency graph approaches infinity (entry into a surface-wave stopband), the counterpart situation in the reflection-phase diagram is a zero-crossing, i.e., AMC or HIS condition. Although no linkage between the two graphs can be detected for the frequency regions of falling propagation-constant values in one and increasingly negative reflection-phase values in the other, it is of no necessity finding any connection since it can be observed from all preceding reflection-phase diagrams that the traces for positive and negative phases are vertically and horizontally flip-symmetric. As such, it suffices to consider just positive values of the reflection-phase. All these foregoing observations constitute the foundational concept on which the subsequent derivation stages rest.

[43] With the above laid out, it would not be difficult to deduce that the reflection phase may assume a reciprocal relation with the propagation constant according to:

$$\angle\Gamma = \pi(2\pi f/c)/k_x \tag{23}$$

noticing how the equality of the reflection-phase to 180° whenever k_x equals the free-space wave number, i.e., when the dispersion curve grazes the light-line, has been enforced as required. However, from our computational experiments, it was found that the traces of the reflection-phase diagram produced by this (23) just decay too slowly from 180° initially with frequency (i.e., initial entry into surface-wave passbands) due to the strong quasi-asymptote of the dispersion trace with the light-line pertaining to initial gentle entry of the surface-wave into the slow-wave region. Nonetheless, as the surface wave moves deeper into the slow-wave region, the rate of increase of its propagation constant with frequency gradually matches up fairly well with the rate of fall of the reflection-phase, thereby suggesting that the reciprocal relationship of (23) can be viable over those frequency ranges (nearer toward the upper edge of each surface-wave passband).

[44] Now, if we take the liberty to break away from the correction term $g/d_x \leq 1$ of (21b) and let it exceed unity to become a new quantity, say $\zeta g/d_x$, it has been observed from our computational experiments that the larger this ζ is, the higher will be the rate of increase of the propagation constant with frequency as the surface-wave initially moves into the slow-wave region. In other words, as each mode preliminarily moves from the fast-wave region into the slow-wave region, the modified trace produced by using the abovementioned new quantity no longer creeps as slowly along the light-line with rising frequency as before the $\zeta > 1$ term was implemented, i.e., reduced lingering on the light-line.

[45] With these above-described aspects, we may write the modified term as

$$\zeta = a_1^{a_2(2\pi f/c)/k_x} \tag{24}$$

with associated

$$k_x^{\text{modif}} = \sqrt{4(\pi f)^2\mu_0\varepsilon_0 + 4\mu_0\varepsilon_0\left(\zeta\frac{g\pi f}{d_x}\right)^2\frac{\mu_{rel,cav}}{\varepsilon_{rel,cav}}\tan^2\left(2\pi f d\sqrt{\mu_{cav}\varepsilon_{cav}}\right)} \tag{25}$$

$$\angle\Gamma^{\text{modif}} = \pi(2\pi f/c)/k_x^{\text{modif}} \tag{26}$$

where $a_1 > 1$ and a_2 are coefficients to be specified later. In this way, when the surface-wave number k_x equals the free-space wave number (dispersion trace touches the light-line, i.e., entry into surface-wave passband, with corresponding flipping of the reflection-phase diagram curve from $-180°$ to $+180°$ and subsequent falling toward zero-phase from 180°), the ζ term assumes the value of $a_1^{a_2} > 1$, being the maximum amplitude of the scaling coefficient where it is needed to 'pull' the dispersion trace off the light-line at a faster rate (with frequency) in order for an associated higher fall-rate of the resultant $\angle\Gamma^{\text{modif}}$of (26) with frequency. Whereas as k_x rises toward infinity (with associated zero-crossing of the reflection-phase), ζ drops to a value closer to unity in accordance with the increasingly matching rate of change between the reflection-phase and dispersion diagrams as mentioned at the end of the paragraph preceding the previous.

6.1. Dependency on Incident Theta Angle

[46] However, the dependency on the incident theta angle of the impingent plane wave (as required by reflection-phase studies) onto the corrugated surface has not yet been considered, i.e., the term θ_{inc} must be incorporated into the functional expression for the reflection phase, the necessity of which being obvious from Figure 6. This variable is absent from the original formula of (21b). Intuitively, the terms a_1 and a_2 of (24) are picked out to be assigned as functions of θ_{inc}, i.e., $a_1(\theta_{inc})$ and $a_2(\theta_{inc})$. Subsequently, the final form of the reflection-phase is anticipated to look like:

$$\angle\Gamma^{\text{final}} = \frac{[\pi + a_0(\theta_{inc})](2\pi f/c)}{k_x^{\text{modif}}(a_1(\theta_{inc}), a_2(\theta_{inc}))} - a_0(\theta_{inc}) \tag{27}$$

whereby a_0 is a new quantity also dependent on θ_{inc}, and the dependency of k_x^{modif} from (25) on ζ of (24) and in turn on $a_1(\theta_{inc})$ and $a_2(\theta_{inc})$ are explicitly shown. The dependency on the rest of the parameters are implicit within k_x^{modif}.

[47] Next, a parametric study of θ_{inc} in terms of the reflection-phase diagram generated using the full-wave rigorous moment-method code is performed, for an arbitrary set of controlled (fixed) values of all the other parameters. The results of this study shall then constitute the reference data needed to determine the functional forms of $a_0(\theta_{inc})$, $a_1(\theta_{inc})$ and $a_2(\theta_{inc})$. To do so, the first step would be to compute $\angle\Gamma^{\text{final}}$ of (27) for the abovementioned controlled values of all parameters (except θ_{inc}) over ranges of values of a_0,

Table 1. Range of Values of the Five Parameters

p_1 (mm)	p_2	p_3	p_4	p_5 (rad)
1	2	2	0.45	0.001745
1.3	3	2.4	0.55	0.30194
1.6	4	2.8	0.65	0.6021
1.9	5	3.2	0.75	0.9023
2.2	6	3.6	0.85	1.2025
2.5	7	4	0.95	1.503

a_1 and a_2; specifically, from 0 to $\pi/6$ for a_0 and 1.725 to 2.6 for both a_1 and a_2, each of them in some number of step-divisions. The plotted graph of every resultant $\angle\Gamma^{\text{final}}$ versus frequency is then checked up with a certain θ_{inc} case from the set of reference graphs of $\angle\Gamma^{\text{MOM}}$ against frequency (where the superscript MOM denotes moment-method), from which the most matching set of (a_0, a_1, a_2) values is selected to be assigned to that θ_{inc} case. Repeating this for all θ_{inc} cases in the reference parametric data set reveals the a_0, a_1 and a_2 as discrete functions of θ_{inc}. For the present example of eighteen θ_{inc} cases in the parametric set, the discretized a_0, a_1 and a_2 are constructed as discrete functions of θ_{inc}. These 18-element vectors of numerical data for a_0, a_1 and a_2 may then be curve-fitted into polynomial functions of θ_{inc} by standard techniques. Upon doing so with a polynomial degree of 5 for decent modeling of the discrete functions, the functional forms of these coefficients are explicitly stated as follow.

$$a_0 = P_0(1)\theta_{inc}^5 + P_0(2)\theta_{inc}^4 + P_0(3)\theta_{inc}^3 + P_0(4)\theta_{inc}^2 + P_0(5)\theta_{inc}^1 + P_0(6) \tag{28a}$$

$$a_1 = P_1(1)\theta_{inc}^5 + P_1(2)\theta_{inc}^4 + P_1(3)\theta_{inc}^3 + P_1(4)\theta_{inc}^2 + P_1(5)\theta_{inc}^1 + P_1(6) \tag{28b}$$

$$a_2 = P_2(1)\theta_{inc}^5 + P_2(2)\theta_{inc}^4 + P_2(3)\theta_{inc}^3 + P_2(4)\theta_{inc}^2 + P_2(5)\theta_{inc}^1 + P_2(6) \tag{28c}$$

where the coefficients of the polynomial functions are placed in 6-element vectors P_0, P_1, and P_2:

$$P_0 = [1.176; -3.097;\ 2.761; -0.9576; 0.1196; -0.001038] \tag{29a}$$

$$P_1 = [2.448; -6.879;\ 6.693; -2.625; 0.3526;\ 1.719] \tag{29b}$$

$$P_2 = [1.415; -6.423;\ 9.239; -4.165; 0.5520;\ 1.717] \tag{29c}$$

[48] With these established, the efficacy of the formula for $\angle\Gamma^{\text{final}}$ in producing the reflection-phase diagrams had been demonstrated in terms of parametric studies; however these results are not presented in this paper due to space constraints. Five parameters for characterizing the corrugations and its impingent excitation plane wave had been considered. They are (a) the period d_x, (b) the relative permittivity of the groove-filling: $\varepsilon_{rel,cav} = \varepsilon_{cav}/\varepsilon_0$, (c) the corrugation-depth to period ratio: h/d_x, (d) the ratio between the width of the cavity (or groove) and the period: g/d_x, and (e) the elevation theta angle of incidence: θ_{inc}. Let us henceforth refer to these five parameters as p_1, p_2, p_3, p_4, and p_5, respectively, for convenience and brevity. Table 1 provides the numerical values of these investigated five parameters, being 6 of them per parameter.

6.2. Inclusion of Incident Phi Angle Variation

[49] In order to include the dependency of the reflection-phase for TM^z polarization on the azimuthal incident angle ϕ_{inc}, a parametric study of the reflection-phase over those aforementioned five parameters (defined as p_1 to p_5) is conducted (again using the full-wave moment method), but now including ϕ_{inc} as the sixth parameter. From the computed reflection-phase diagrams (not presented here due to the voluminous size), comparison by observation of the reflection-phase diagram between the $\phi_{inc} = 0$ case (being the situation thus-far considered, i.e., propagation in the plane perpendicular to the corrugations) and that of a nonzero ϕ_{inc} case for a certain common set of the other (five) parameters (period, groove permittivity, depth, width, and θ_{inc}) reveals frequency shifting between the two traces, the amount of deviation being a function of frequency (increases with it). Repeating such a comparison for another θ_{inc} case, it is found that this frequency shift also grows with θ_{inc}, but slowly for initially small θ_{inc} values (near broadside incidence), becoming increasingly appreciable as the incident plane wave gets closer to grazing. Repeating these comparisons yet for another ϕ_{inc} case shows that the frequency shift also varies with the azimuthal incidence angle. Hence, this frequency shift is a function of three parameters: (a) frequency, (b) θ_{inc}, and (c) ϕ_{inc}. Interestingly, this shift does not depend on the other four physical properties of the corrugations. Again in a similar way to the modeling of the coefficients a_0, a_1 and a_2 earlier on as polynomial functions, the frequency shift can also be modeled as an analytic polynomial function of those three parameters using the numerical data generated by the parametric study. The considered ranges of the three parameters are as follow: (a) five values of ϕ_{inc}: 0.1°, 22.55°, 45°, 67.45°, and 89.9°; (b) eight values of θ_{inc}: 0.1°, 10.85°, 21.6°, 32.35°, 43.1°, 53.85°, 64.6°, and 75.35°; and (c) nine values of frequency f: 5 GHz, 10 GHz, 15 GHz, 20 GHz, 25 GHz, 30 GHz, 35 GHz, 40 GHz, and 45 GHz. For convenience, we shall henceforth use serial indices to denote any of these values, e.g., ϕ_{inc}#3 = 45°, θ_{inc}#5 = 43.1°, f#7 = 35 GHz, etc.

[50] Performing the polynomial curve-fitting for a degree of 2, i.e., a quadratic-equation modeling, the frequency shift of the reflection-phase diagram trace for any nonzero ϕ_{inc} case (but sharing the same set of the other parameters of the $\phi_{inc} = 0$ case) from that of the $\phi_{inc} = 0$ case may be expressed as

$$f_{shift}\left(\hat{\phi}_{inc}, \hat{\theta}_{inc}, \hat{f}\right) = \left(C_{\phi^2\theta^2}\hat{\theta}_{inc}^2 + C_{\phi^2\theta^1}\hat{\theta}_{inc} + C_{\phi^2\theta^0}\right)\hat{\phi}_{inc}^2 + \left(C_{\phi^1\theta^2}\hat{\theta}_{inc}^2 + C_{\phi^1\theta^1}\hat{\theta}_{inc} + C_{\phi^1\theta^0}\right)\hat{\phi}_{inc} + \left(C_{\phi^0\theta^2}\hat{\theta}_{inc}^2 + C_{\phi^0\theta^1}\hat{\theta}_{inc} + C_{\phi^0\theta^0}\right) \tag{30a}$$

$C_{\phi^2\theta^2 f^2} = -10.765$	$C_{\phi^2\theta^2 f^1} = -3.7347$	$C_{\phi^2\theta^2 f^0} = 13.6473$
$C_{\phi^2\theta^1 f^2} = -32.6655$	$C_{\phi^2\theta^1 f^1} = -37.446$	$C_{\phi^2\theta^1 f^0} = 7.2428$
$C_{\phi^2\theta^0 f^2} = -23.861$	$C_{\phi^2\theta^0 f^1} = -31.006$	$C_{\phi^2\theta^0 f^0} = 3.35174$

$C_{\phi^1\theta^2 f^2} = -11.0652$	$C_{\phi^1\theta^2 f^1} = 14.62565$	$C_{\phi^1\theta^2 f^0} = 66.41$
$C_{\phi^1\theta^1 f^2} = -78.403$	$C_{\phi^1\theta^1 f^1} = 127.291$	$C_{\phi^1\theta^1 f^0} = 417.97$
$C_{\phi^1\theta^0 f^2} = -84.145$	$C_{\phi^1\theta^0 f^1} = 189.0554$	$C_{\phi^1\theta^0 f^0} = 504.24$

$C_{\phi^0\theta^2 f^2} = -23.844$	$C_{\phi^0\theta^2 f^1} = 7.259$	$C_{\phi^0\theta^2 f^0} = 65.158$
$C_{\phi^0\theta^1 f^2} = -91.067$	$C_{\phi^0\theta^1 f^1} = 156.555$	$C_{\phi^0\theta^1 f^0} = 447.7108$
$C_{\phi^0\theta^0 f^2} = -75.586$	$C_{\phi^0\theta^0 f^1} = 127.16$	$C_{\phi^0\theta^0 f^0} = 376.872$

Figure 8. Coefficients of equations (30a) and (30b). All values are normalized to 10^6.

where any $C_{\phi^u\theta^v}$ is in turn a polynomial (quadratic) function of $\hat{f}$, i.e.

$$C_{\phi^u\theta^v}\left(\hat{f}\right) = C_{\phi^u\theta^v f^2}\hat{f}^2 + C_{\phi^u\theta^v f^1}\hat{f} + C_{\phi^u\theta^v f^0} \tag{30b}$$

for all combination-pairs of (u, v) in (30a), and whereby

$$\hat{\phi}_{inc} = \left(\phi_{inc} - \mu_\phi\right)/\sigma_\phi \tag{31a}$$

$$\hat{\theta}_{inc} = \left(\theta_{inc} - \mu_\theta\right)/\sigma_\theta \tag{31b}$$

$$\hat{f} = \left(f - \mu_f\right)/\sigma_f \tag{31c}$$

where μ and σ are the mean and standard deviation of the parameter denoted by their respective subscripts. For our range of parametric values stated above, these are: $\mu_\phi = 0.7854$, $\sigma_\phi = 0.61953$; $\mu_\theta = 0.6584$, $\sigma_\theta = 0.45958$; $\mu_f = 2.5 \times 10^{10}$, $\sigma_f = 1.3693 \times 10^{10}$. The numerical values of the coefficients $C_{\phi^u\theta^v f^w}$ of (30b), where u, v, and w may denote 2, 1 or 0, are tabulated in Figure 8.

[51] Therefore, the *ultimate* explicit formula for the reflection phase as an entirely closed-form analytic function of *all parameters* of the corrugations, incident plane wave (particularly now with even ϕ_{inc} included), and the frequency is stated as:

$$\angle\Gamma^{\text{ultim}} = \frac{[\pi + a_0(\theta_{inc})](2\pi f'/c)}{k^{\text{modif}}_{x_{\text{ultim}}}(a_1(\theta_{inc}), a_2(\theta_{inc}))} - a_0(\theta_{inc}) \tag{32a}$$

from (27), in which a_0, a_1 and a_2 those of (28a), (28b) and (28c), and with

$$k^{\text{modif}}_{x_{\text{ultim}}} = \sqrt{4(\pi f')^2\mu_0\varepsilon_0 + 4\mu_0\varepsilon_0\left(\zeta'\frac{g\pi f'}{d_x}\right)^2\frac{\mu_{rel,cav}}{\varepsilon_{rel,cav}}\tan^2\left(2\pi f' d\sqrt{\mu_{cav}\varepsilon_{cav}}\right)} \tag{32b}$$

from (25), where

$$\zeta' = a_1^{a_2(2\pi f'/c)/k'_x} \tag{32c}$$

from (24), in which a_1 and a_2 are those of (28b) and (28c), and with

$$k'_x = \sqrt{4(\pi f')^2\mu_0\varepsilon_0 + 4\mu_0\epsilon_0\left(\frac{g\pi f'}{d_x}\right)^2\frac{\mu_{rel,cav}}{\varepsilon_{rel,cav}}\tan^2\left(2\pi f' d\sqrt{\mu_{cav}\varepsilon_{cav}}\right)} \tag{32d}$$

from (21b), and of course finally, with the shifted frequency:

$$f' = \left(f - f_{shift}\right) \tag{32e}$$

where f_{shift} is from (30a) and is a function of ϕ_{inc}, θ_{inc} and f.

[52] The ultimate results for the demonstration of the efficacy of equations (32a)–(32e) are now presented in Figure 9 for five cases of entirely arbitrary parameters. Each graph within this figure contains the reflection-phase diagram generated by equations (32a)–(32e) and the rigorous full-wave moment method formulated in section 2. Clearly, the agreement between the two approaches is seen to be outstanding. The CPU times for both were also computed and the derived formula is found to be around 40 times faster than the moment method.

7. Further Extension to TE^z Polarized Incidence

[53] The same procedure as before for TM^z can be repeated for deriving a formula for the phase of the $E_{x,refl}/E_{x,inc}$ reflection coefficient for TE^z modes, but with the only difference now being in the modeling of the variation with θ_{inc}. In other words, we anticipate that the same final formula of (32a)–(32e) may reapply, but just with modifications of a_0, a_1 and a_2 in which the dependency on θ_{inc} lies. Such inheritance of the functional variation of the TE^z reflection-phase with all other parameters aside from θ_{inc} from the TM^z case may on the outset appear to be rather speculative. It however turns out to be actually correct and is thus a well-taken risk that constitutes a vital discovery. Continuing with the description of the procedure, similar to the former TM^z case, a parametric study of θ_{inc} in terms of the reflection-phase diagram generated using the full-wave rigorous moment-method code is first performed, for an arbitrary set of controlled (fixed) values of all the other parameters. The results of this study shall then constitute the reference data needed to determine the functional forms of $a_0(\theta_{inc})$, $a_1(\theta_{inc})$ and $a_2(\theta_{inc})$. However, now for TE^z modes, it is found that a proper modeling can be achieved with only a_2 varying with θ_{inc}, whereas both a_0 and a_1 are now being fixed constants:

$$a_0^{TE} = -\pi/18 \tag{33a}$$

$$a_1^{TE} = 1.8 \tag{33b}$$

[54] These values were obtained by numerical experimentations and thus do not bear significance of exactness. As before, a_2 can be obtained as a discrete function of θ_{inc}. Although a total of eighteen θ_{inc} cases ranging from 0 to 90° have been considered in the parametric set as was for TM^z case earlier, the discretized a_2 as a function of θ_{inc} is

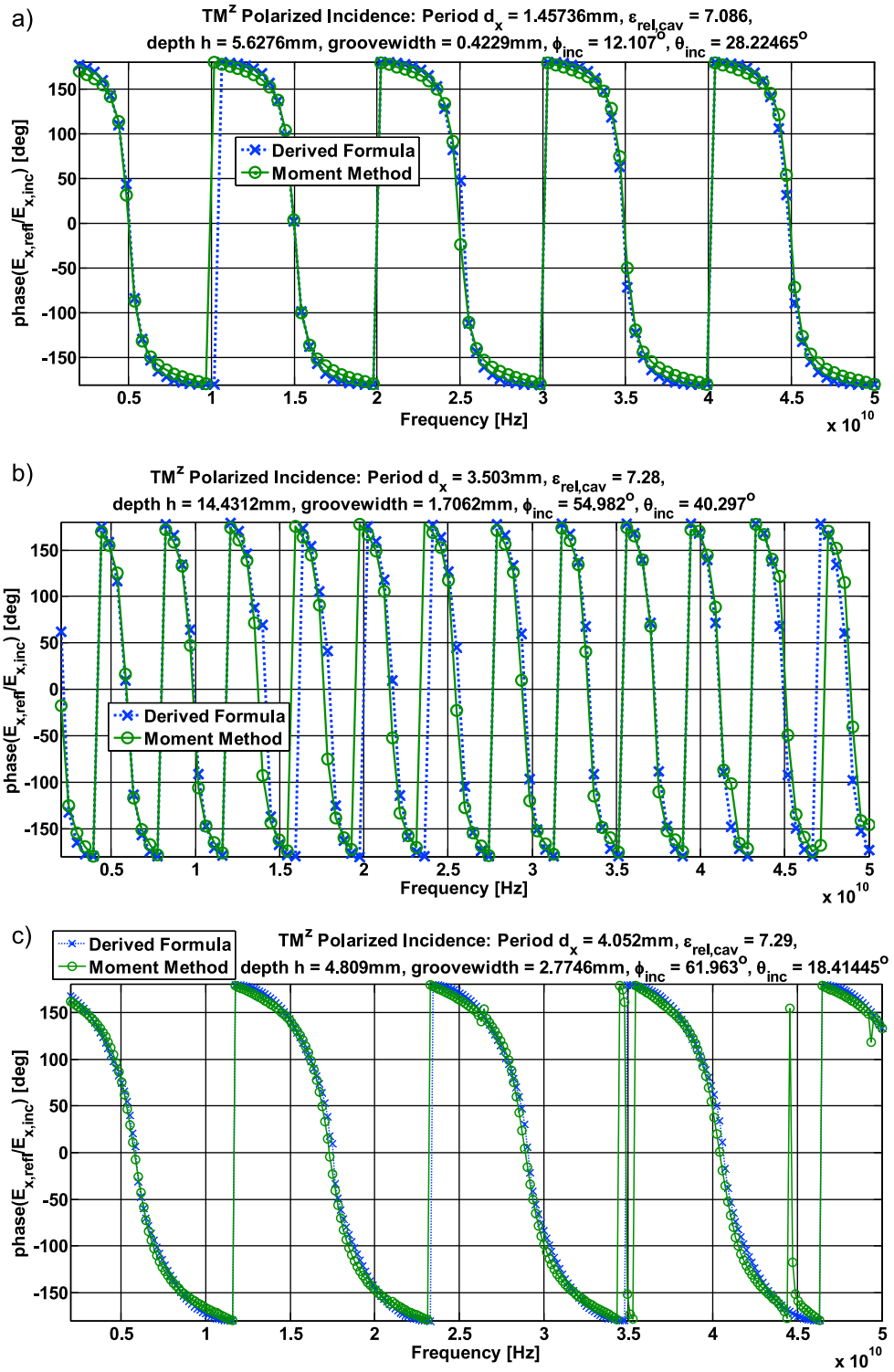

Figure 9. Reflection phase diagrams for five arbitrary examples, generated by derived formula (32a)–(32e) and validated by full-wave moment method, both for TM^z polarization: (a) d_x = 1.45736 mm, $\varepsilon_{rel,cav}$ = 7.086, h = 5.6276 mm, g = 0.4229 mm, ϕ_{inc} = 12.107°, θ_{inc} = 28.22465°; (b) d_x = 3.503 mm, $\varepsilon_{rel,cav}$ = 7.28, h = 14.4312 mm, g = 1.7062 mm, ϕ_{inc} = 54.982°, θ_{inc} = 40.297°; (c) d_x = 4.052 mm, $\varepsilon_{rel,cav}$ = 7.29, h = 4.809 mm, g = 2.7746 mm, ϕ_{inc} = 61.963°, θ_{inc} = 18.41445°; (d) d_x = 1.065 mm, $\varepsilon_{rel,cav}$ = 5.218, h = 2.98638 mm, g = 0.2498 mm, ϕ_{inc} = 84.1824°, θ_{inc} = 32.9185°; and (e) d_x = 5.9925 mm, $\varepsilon_{rel,cav}$ = 6.712, h = 16.7716 mm, g = 1.5288 mm, ϕ_{inc} = 55.551°, θ_{inc} = 32.8664°.

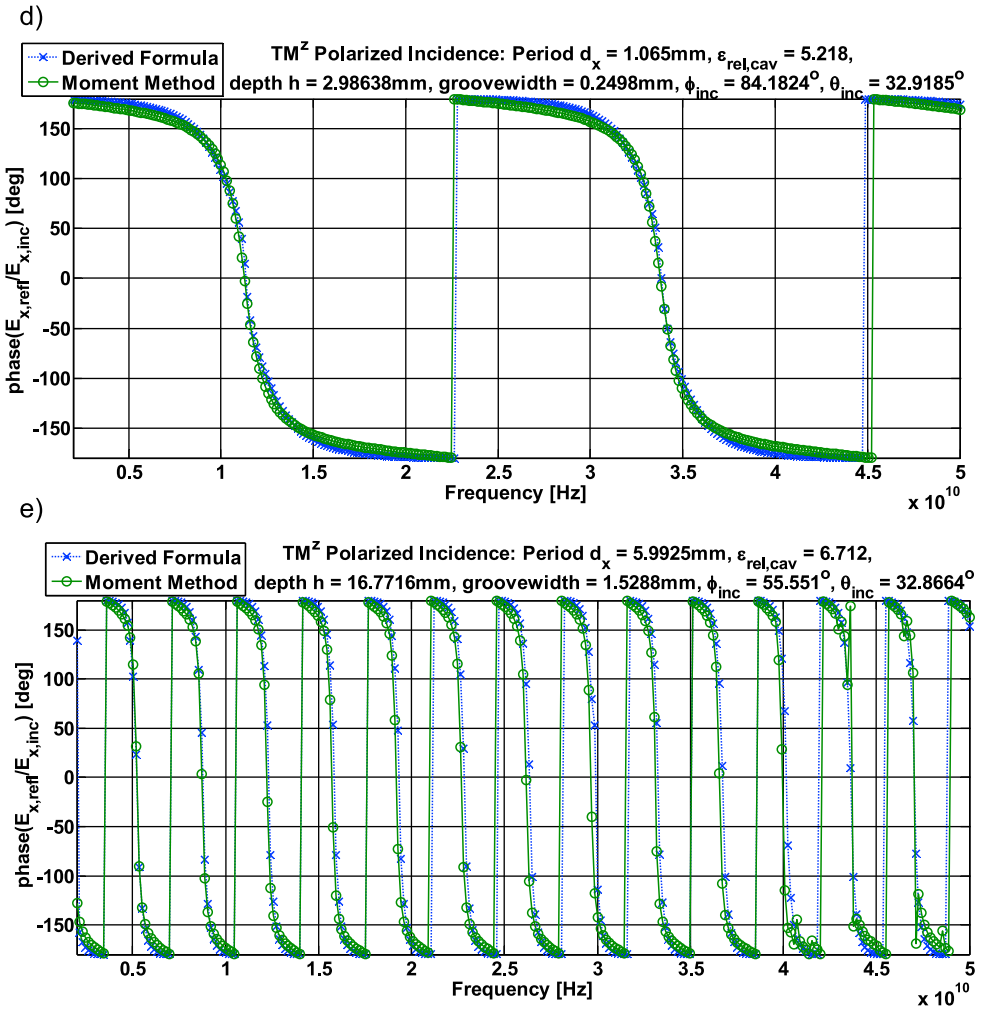

Figure 9. (continued).

constructed with only the first ten θ_{inc} values ranging from 0 to about 45° (0.7854 radians), because the concept of frequency bands with positive and negative phase values corresponding respectively to surface-wave passbands and stopbands holds only if θ_{inc} is not too large for TE^z case. Hence, the upcoming derived formula is valid only up to θ_{inc} = 45°. This 10-element vector of numerical data for a_2 may be curve-fitted into a simple quadratic (polynomial degree 2) function of θ_{inc} again by standard techniques. Upon doing so, the functional form of a_2 is explicitly stated as follow.

$$a_2^{TE}(\theta_{inc}) = P_2^{TE}(1)\theta_{inc}^2 + P_2^{TE}(2)\theta_{inc}^1 + P_2^{TE}(3) \tag{33c}$$

where the coefficients of the quadratic function are placed in the 3-element vector P_2^{TE}:

$$P_2^{\mathrm{TE}} = [-1.418844;\ 0.09376458;\ 1.603313163] \tag{34}$$

[55] Subsequently, the ultimate form of the mostly inherited explicit formula (from the TM^z case) for the reflection-phase of TE^z modes as a closed-form analytic function of all parameters of the corrugations, incident plane wave and frequency is stated as (modified from (32a)–(32e)):

$$\angle\Gamma^{\mathrm{ultim}} = \frac{\left[\pi + a_0^{TE}\right](2\pi f'/c)}{k_{x_{\mathrm{ultim}},TE}^{\mathrm{modif}}\left(a_1^{TE}, a_2^{TE}(\theta_{inc})\right)} - a_0^{TE} \tag{35a}$$

from (32a), in which a_0^{TE} is of (33a), and with

$$k_{x_{\mathrm{ultim}},TE}^{\mathrm{modif}} = \sqrt{4(\pi f')^2\mu_0\varepsilon_0 + 4\mu_0\varepsilon_0\left(\zeta'_{TE}\frac{g\pi f'}{d_x}\right)^2\frac{\mu_{rel,cav}}{\varepsilon_{rel,cav}}\tan^2\left(2\pi f' d\sqrt{\mu_{cav}\varepsilon_{cav}}\right)} \tag{35b}$$

from (32b), where

$$\zeta'_{TE} = \left(a_1^{TE}\right)^{a_2^{TE}(2\pi f'/c)/k'_x} \tag{35c}$$

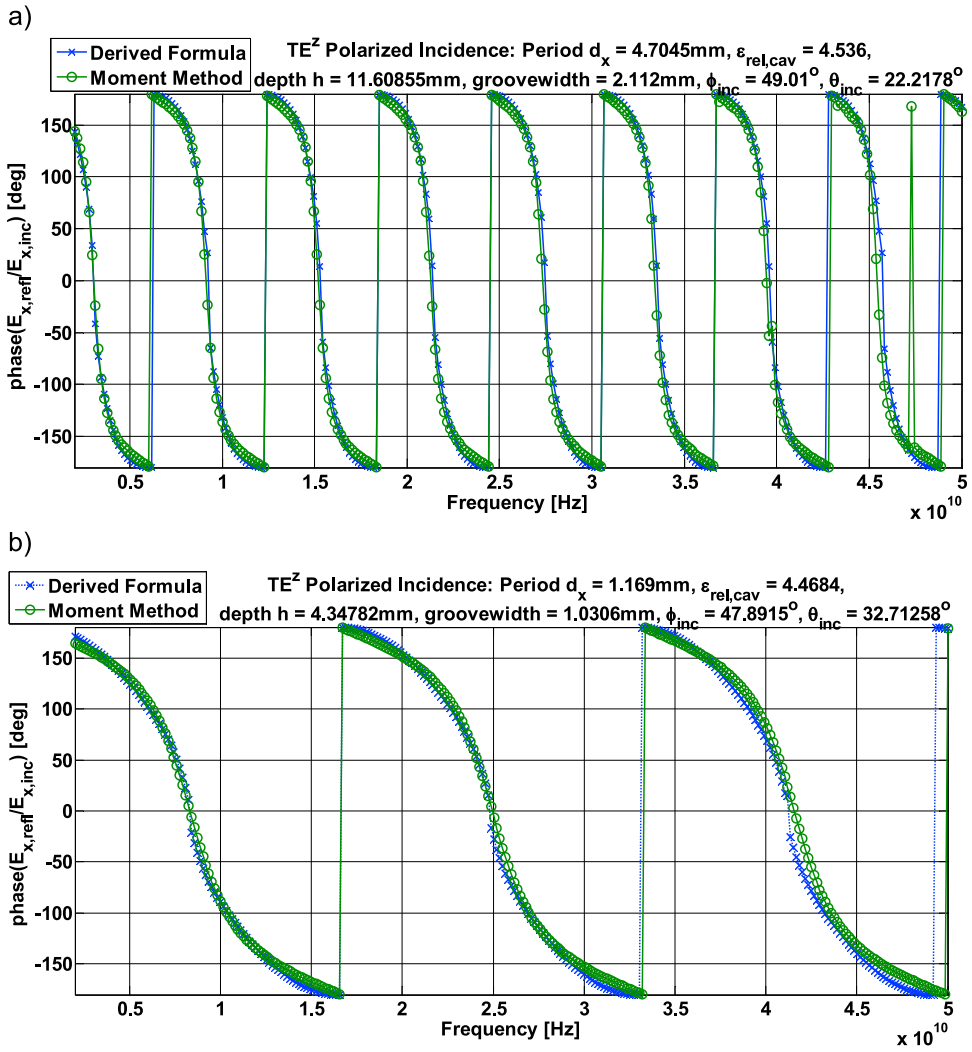

Figure 10. Reflection phase diagrams for two arbitrary examples, generated by derived formula (35a)–(35e) and validated by full-wave moment method, both for TM^z polarization: (a) d_x = 4.7045 mm, $\varepsilon_{rel,cav}$ = 4.536, h = 11.60855 mm, g = 2.112 mm, ϕ_{inc} = 49.01°, θ_{inc} = 22.2178° and (b) d_x = 1.169 mm, $\varepsilon_{rel,cav}$ = 4.4684, h = 4.34782 mm, g = 1.0306 mm, ϕ_{inc} = 47.8915°, θ_{inc} = 32.71258°.

from (32c), in which a_1^{TE} and $a_2^{TE}(\theta_{inc})$ are of (33b) and (33c), and where k'_x is the same one as of (32d), repeated here for convenience and clarity,

$$k'_x = \sqrt{4(\pi f')^2\mu_0\varepsilon_0 + 4\mu_0\varepsilon_0\left(\frac{g\pi f'}{d_x}\right)^2 \frac{\mu_{rel,cav}}{\varepsilon_{rel,cav}} \tan^2\left(2\pi f' d\sqrt{\mu_{cav}\varepsilon_{cav}}\right)} \tag{35d}$$

and of course finally, with the same shifted frequency of (32e), also repeated here:

$$f' = \left(f - f_{shift}\right) \tag{35e}$$

where f_{shift} is also from (30a) and is a function of ϕ_{inc}, θ_{inc} and f.

[56] The ultimate results for the demonstration of the efficacy of equations (35a)–(35e) for TE^z modes are now presented in Figure 10, now for two entirely arbitrary sets of parameters. As before, each graph contains the reflection-phase diagram generated by equations (35a)–(35e) and the rigorous full-wave moment method formulated in section 2. Clearly, the agreement between the two approaches is again seen to be excellent for this TE^z case. And comparing the processor times of these two approaches, the formula of (35a)–(35e) is found to be around 56 times faster than the moment method, a larger speedup than TM^z modes, interestingly.

8. Conclusions

[57] Planar corrugated surfaces play an important role in today's world of microwave devices and antennas by presenting themselves as either artificial magnetic conducting (AMC) or electromagnetic bandgap (EBG) surfaces. The key aspect that characterizes the high-impedance surface properties is the phase of the reflection coefficient (or reflection-phase), which for both TE and TM polarized incident plane waves, allows for complete characterization. In spite of its importance, nowhere in the existing literature may a closed-form analytic formula for this reflection-phase for both TE

and TM polarization as an explicit function of all parameters be found, especially including the dependency on the azimuth angle of incidence ϕ_{inc}. This work has resolved this: explicit formulas for both TE and TM reflection phase as closed-form analytic functions of all parameters of the corrugations and the incident plane wave have been derived. As demonstrated, immense speedup in computational time over a full-wave approach with the method of moments by over 40 times is afforded. This strongly facilitates rapid designs of AMC surfaces using such planar corrugations, especially when the extent of the parametric-space to be searched for the optimal design is large. It is believed that these formulas shall become a powerful tool for industrial designers and academic research engineers alike.

[58] **Acknowledgment.** This work has been funded by the National Science Council of Taiwan (NSC 100-2221-E-009-142)

References

Alfonso, E., A. Valero-Nogueira, J. I. Herranz, and F. Vico (2009), Moment method analysis of corrugated surfaces using the aperture integral equation, *IEEE Trans. Antennas Propag.*, *57*(7), 2208–2212, doi:10.1109/TAP.2009.2021976.

Elliott, R. S. (1954), On the theory of corrugated plane surfaces, *IRE Trans. Antennas Propag.*, *2*, 71–81.

Farahani, H. S., M. Veysi, M. Kamyah, and A. Tadjalli (2010), Mutual coupling reduction in patch antenna arrays using a UC-EBG superstrate, *IEEE Antennas Wireless Propag. Lett.*, *9*, 57–59, doi:10.1109/LAWP.2010.2042565.

Foroozesh, A., L. Shafai, and M. Ng Mou Kehn (2008a), Application of polarization and angular dependent artificial ground planes in compact planar high-gain antenna design, *Radio Sci.*, *43*, RS6S03, doi:10.1029/2007RS003795.

Foroozesh, A., M. Ng Mou Kehn, and L. Shafai (2008b), Application of artificial ground planes in dual-band orthogonally-polarized low-profile high-gain planar antenna design, *Prog. Electromagn. Res.*, *84*, 407–436, doi:10.2528/PIER08062804.

Goldstein, H. (1943), Cavity resonators and waveguides containing periodic elements, PhD thesis, Mass. Inst. of Technol., Cambridge.

Goldstein, H. (1944), The theory of corrugated transmission lines and waveguides, *Rep. 494*, pp. 1–17, Radiat. Lab., Mass. Inst. of Technol., Cambridge.

Goubau, G. (1950), Surface waves and their application to transmission lines, *J. Appl. Phys.*, *21*, 1119–1128, doi:10.1063/1.1699553.

Goussetis, G., A. P. Feresidis, and J. C. Vardaxoglou (2006), Tailoring the AMC and EBG characteristics of periodic metallic arrays printed on grounded dielectric substrate, *IEEE Trans. Antennas Propag.*, *54*(1), 82–89, doi:10.1109/TAP.2005.861575.

Hanninen, I., and K. Nikoskinen (2008), Implementation of method of moments for numerical analysis of corrugated surfaces with impedance boundary condition, *IEEE Trans. Antennas Propag.*, *56*(1), 278–281, doi:10.1109/TAP.2007.913171.

Hougardy, R. W., and R. C. Hansen (1958), Scanning surface wave antennas – oblique surface waves over a corrugated conductor, *IRE Trans. Antennas Propag.*, *6*, 370–376, doi:10.1109/TAP.1958.1144619.

Kalhor, H. A. (1976), Numerical evaluation of Rayleigh hypothesis for analyzing scattering from corrugated gratings—TE polarization, *IEEE Trans. Antennas Propag.*, *24*, 884–889, doi:10.1109/TAP.1976.1141432.

Kalhor, H. A. (1977), Approximate analysis of electromagnetic scattering from corrugating conducting surfaces by surface impedance modeling, *IEEE Trans. Antennas Propag.*, *25*, 721–722, doi:10.1109/TAP.1977.1141674.

Kamgaing, T., and O. M. Ramahi (2008), Multiband electromagnetic-bandgap structures for applications in small form-factor multichip module packages, *IEEE Trans. Microwave Theory Tech.*, *56*(10), 2293–2300, doi:10.1109/TMTT.2008.2003525.

Kildal, P.-S. (1990), Artificially soft and hard surfaces in electromagnetics, *IEEE Trans. Antennas Propag.*, *38*(10), 1537–1544, doi:10.1109/8.59765.

Kim, J. P., C. W. Lee, and H. Son (1999), Analysis of corrugated surface wave antenna using hybrid MOM/UTD technique, *Electron. Lett.*, *35*(5), 353–354, doi:10.1049/el:19990144.

Kriegsmann, G. A., and B. K. McCartin (1996), Scattering by a rectangularly corrugated surface: an approximate theory, *IEEE Trans. Antennas Propag.*, *44*(8), 1193–1194, doi:10.1109/8.511829.

Li, R., G. DeJean, M. M. Tentzeris, J. Papapolymerou, and J. Laskar (2005), Radiation-pattern improvement of patch antennas on a large-size substrate using a compact soft-surface structure and its realization on LTCC multilayer technology, *IEEE Trans. Antennas Propag.*, *53*(1), 200–208, doi:10.1109/TAP.2004.840754.

Mohajer-Iravani, B., and O. M. Ramahi (2007), Suppression of EMI and electromagnetic noise in packages using embedded capacitance and miniaturized electromagnetic bandgap structures with high-k dielectrics, *IEEE Trans. Adv. Packag.*, *30*(4), 776–788, doi:10.1109/TADVP.2007.908028.

Mohajer-Iravani, B., S. Shahparnia, and O. M. Ramahi (2006), Coupling reduction in enclosures and cavities using electromagnetic band gap structures, *IEEE Trans. Electromagn. Compat.*, *48*(2), 292–303, doi:10.1109/TEMC.2006.874666.

Ng Mou Kehn, M., M. Nannetti, A. Cucini, S. Maci, and P.-S. Kildal (2006), Analysis of dispersion in dipole-FSS loaded hard rectangular waveguide, *IEEE Trans. Antennas Propag.*, *54*(8), 2275–2282, doi:10.1109/TAP.2006.879198.

Piefke, G. (1959), The transmission characteristics of a corrugated guide, *IRE Trans. Antennas Propag.*, *7*, 183–190, doi:10.1109/TAP.1959.1144740.

Sievenpiper, D. F., L. Zhang, R. F. Jimenez Broas, N. G. Alexopoulos, and E. Yablonovitch (1999), High-impedance electromagnetic surfaces with a forbidden frequency band, *IEEE Trans. Microwave Theory Tech.*, *47*(11), 2059–2074, doi:10.1109/22.798001.

Sipus, Z., P.-S. Kildal, R. Leijon, and M. Johansson (1998), An algorithm for calculating Green's functions of planar, circular cylindrical, and spherical multilayer structures, *Appl. Comput. Electromagn. Soc. J.*, *13*(3), 243–254.

Sommerfeld, A. (1909), Über die Ausbreitung der Wellen in der drahtlosen Telegraphie, *Ann. Phys.*, *333*(4), 665–736, doi:10.1002/andp.19093330402.

Uusitupa, T. M. (2006), Usability studies on approximate corrugation models in scattering analysis, *IEEE Trans. Antennas Propag.*, *54*(9), 2486–2496, doi:10.1109/TAP.2006.880774.

Yang, F., and Y. Rahmat-Samii (2003), Microstrip antennas integrated with electromagnetic band-gap (EBG) structures: a low mutual coupling design for array applications, *IEEE Trans. Antennas Propag.*, *51*(10), 2936–2946, doi:10.1109/TAP.2003.817983.

Yang, F., and Y. Rahmat-Samii (2008), *Electromagnetic Band Gap Structures in Antenna Engineering*, Cambridge Univ. Press, Cambridge, U. K., doi:10.1017/CBO9780511754531.